Construction and Building Materials 229 (2019) 116797

Contents lists available at ScienceDirect

Construction and Building Materials

journal homepage: www.elsevier.com/locate/conbuildmat

Multi-level homogenization for the prediction of the mechanical properties of ultra-high-performance concrete

Bezawit F. Haile [a], D.W. Jin [a], Beomjoo Yang [b], Solmoi Park [a], H.K. Lee [a,*]

[a] Department of Civil and Environmental Engineering, Korea Institute of Science and Technology (KAIST), 291 Daehak-ro, Yuseong-gu, Daejeon 34141, Republic of Korea
[b] School of Civil Engineering, Chungbuk National University, 1 Chungdae-ro, Seowon-gu, Cheongju, Chungbuk 28644, Republic of Korea

HIGHLIGHTS

- A multi-level micromechanics based homogenization scheme is developed.
- A combined Molecular dynamics simulation and micromechanics models were adopted.
- Effects of fiber type, geometry, orientation and interface are parametrically studied.
- Compressive strength test, MIP and SEM analysis were conducted.
- Model input parameters were obtained from literature and the experimental program.

ARTICLE INFO

Article history:
Received 24 April 2019
Received in revised form 22 July 2019
Accepted 23 August 2019
Available online 9 September 2019

Keywords:
Ultra-high-performance concrete (UHPC)
Micromechanics
Molecular dynamics
Elastic moduli
Multi-level homogenization

ABSTRACT

Ultra-high-performance concrete (UHPC), a multi-level cementitious composite that has properties influenced by constituents existing at different length scales, requires the combination of different modeling strategies to capture and understand its effective property. A multi-level (six levels) micromechanics-based homogenization is proposed to investigate the elastic mechanical properties of UHPC. Molecular dynamics and micromechanical theories based on Eshelby's inclusion model are adopted to investigate the effects of the properties of the various constituents, such as the fiber type, volume fraction, orientation, geometry, including the size and volume fraction of coarse aggregates on the elastic mechanical properties of UHPC. Experimental investigations incorporating a compressive strength test, scanning electron microscopy, and mercury intrusion porosimetry tests were conducted to validate the model. The proposed multi-level homogenization scheme is able to quantitatively prove the importance of each constituent and provide a modeling tool capable of facilitating a thorough investigation of the mechanical properties of UHPC.

1. Introduction

The development of ultra-high performance concrete (UHPC) came about inthe past four decades after the advancement of reactive powder concrete [1–2]. Since its discovery, UHPC has made a remarkable impact in the construction industry owing to its superior performance [3–5]. UHPC offers increased tensile strength, ductility, compressive strength, toughness and durability against chemical attacks, and resistance to harsh environmental conditions [3–6]. These properties allow for the construction of long-span flexural structural members and lightweight bridge decks, in addition to construction projects involving structures that require high strength materials.

The compressive strength, tensile strength, and elastic modulus are the main properties that affect the structural performance of UHPC. However, accurate determination of the above-mentioned mechanical properties is difficult because of the complexity of the microstructure formed when hydration of the cementitious composites occurs [7]. Researchers seeking to understand the complex microstructural interaction and properties of these intricate cementitious composites have mainly opted towards experimental investigations. These studies involved parametric analysis by changing the volume fraction, fiber orientation, and aspect ratio of fibers [8–15] or focused on the effects of fiber types and different geometries of the fibers [16–19]. Even though several experimental studies, including scanning electron microscopy (SEM) and nano-indentation techniques, have been used to investigate these materials, there are still knowledge gaps on the mechanics of the materials [8–10,15,20–25]. Hence, it is necessary to apply

* Corresponding author.
E-mail address: haengki@kaist.ac.kr (H.K. Lee).

https://doi.org/10.1016/j.conbuildmat.2019.116797
0950-0618/

alternative analysis and investigative models such as multi-scale modeling schemes to predict the performance of UHPC under varying conditions.

A multiscale modeling scheme allows investigation of UHPC at each length scale, which is necessary for materials with significant heterogeneities at different length scales [26,27]. Macroscopic material properties such as elastic moduli and mechanical strength are mainly the effects of mechanisms that happen at smaller length scales such as micro crack interactions [26,28,29]. Hence, a multiscale analysis should incorporate and combine the modeling of the material properties at the nanoscale (10^{-9} m), microscale (10^{-6} m), mesoscale (10^{-3} m), and finally the macroscale [30,31].

A recent work by Contrafatto et al. [27] focused on developing a meso-scale model for concrete by considering it as a multi-phase material. Several other researchers applied micromechanics to model the microstructure of cementitious composites. For instance, Li et al. [32] applied the principles of micromechanics to study the effect of aggregates on the performance of concretes. In another work, the effective Young's modulus of concrete with different aggregate gradation was determined by combining a four-phase composite sphere micromechanical model, which takes into account the presence of interfacial transition zone (ITZ) [33]. For low w/c ratio concretes such as UHPC, even though the thickness of the ITZ is quite small, its effect on elastic properties of the material can be significant depending on the aggregate type [34]. Hence it is important to study these effects in depth using the appropriate multi-scale modeling scheme.

Over the years, several multiple homogenization schemes have been developed in order to determine the properties of cementitious composites at different scales. Al. A. Ostaz et al. [35] combined molecular dynamics (MD) and micromechanics to determine the effective properties of normal strength concrete, while Constantinides and Ulm [36], combined nano-indentation and a two-step micromechanics to determine the effective mechanical properties of concrete. For the modeling of the hydration product C-S-H, Tennis and Jennings [37] first hypothesized the existence of two distinct forms of C-S-H based on nitrogen adsorption and later other researchers verified the merit of this modeling by using Nano indentation techniques [36], NMR relaxometery [38] and specific precipitation space which controls the formation of C-S-H with varying densities based on the available precipitation space and degree of hydration [39]. Moreover, several micromechanical homogenization works have also focused on strength upscaling of cementitious composites to determine the compressive strength, tensile strength and stress stress–strain relationships and failure modes of the material [40–42].

In addition, Sorelli et al. [19], Silva et al. [43], and Zhang et al. [44] demonstrated a micromechanics-based multi-level homogenization scheme that enabled them to investigate the mechanical properties of UHPC, high performance concrete, and hybrid fiber reinforced concretes, respectively. These studies applied a combination of micromechanics and experimental techniques to obtain input parameters at different levels and demonstrated the suitability of micromechanics to predict the properties of cementitious composites [20,35,36]. Zhang et al. [45], utilized the very useful ensemble-volume averaging micromechanics method to develop a three level homogenization scheme for hybrid fiber reinforced concretes. While their scheme can successfully be used to determine the elastic properties of fiber reinforced concretes, due to the significant difference in the microstructure of UHPC from other fiber reinforced concretes, the direct application of the model to UHPC would not be appropriate. In addition, Zhang's model consists of only three levels for the homogenizations steps, however, for UHPC, due to the complexity of the microstructure and the presence of inclusions at several length scales that gives the material the very high packing density, more homogenization step should be added.

Hence, this prompted us to develop a more specific multiscale, multi-level homogenization modeling scheme that can help to predict the constitutive and mechanical properties of UHPC. To clearly capture the microstructural properties of UHPC from other concretes, the scheme applies a combination of molecular dynamics (MD) and micromechanics models based on the Mori-Tanaka method [46], ensemble volume averaging technique (EVA) [47] and composite sphere model [48], the details of which will be discussed in subsequent sections, to consider the various important phases present at the different length scales of the material. This work also includes a parametric study to investigate the effects of the fiber type, fiber geometry (aspect ratio), spatial alignment (randomly oriented or aligned), the effect of adding coarse aggregates of variable size and volume fraction. In addition, the properties of internal damage such as voids in the cementitious composite and the interfacial properties between the fibers, aggregates, and cement paste are investigated. Finally, the predictions of the present model are compared and validated with experimental investigations.

2. Theoretical background

This study implements a multi-level homogenization approach to investigate the mechanical properties of UHPC. The proposed multi-level homogenization consists of 1) MD simulations to determine the mechanical properties of the hydration products, 2) a combination of SEM and mercury intrusion porosimetry (MIP) to determine qualitatively the various phases present in the hydrated concrete, and 3) a multi-level micromechanical homogenization scheme to obtain the effective properties of the cementitious composites at various length scales. Fig. 1 shows a flow diagram with the general steps of the multiscale modeling approach and the multi-level homogenization performed in this study.

At Level I, the multi-level homogenization starts with MD simulations conducted on the crystal structures of the hydration products [37,38]. In this study, an MD simulation conducted on the Materials studio modeling and simulation environment using a micro-canonical ensemble with a constant number of atoms, temperature, and pressure is utilized to determine the elastic mechanical properties of the major hydration products in UHPC. The issue of how to model the structure of C-S-H has been an ongoing scientific dilemma with several researchers suggesting various models. Some have opted towards modeling the C-S-H as amorphous while other argue its more crystalline, hence making it possible to use the crystal structures of the calcium silicate minerals, jennite ($Ca_9Si_6O_{18}(OH)_6{\cdot}8H_2O$) or tobermorite 14 Å ($Ca_5Si_6O_{16}(OH)_2{\cdot}7H_2O$), which are considered very similar to C-S-H [49,50]. In addition, according to a more recent study by Abdolhosseini Qomi et al. [51], at low Ca/Si ratios (Ca/Si less than 1.2) C-S-H exhibits a lamellar crystalline structures, while the structure of C-S-H at high Ca/Si ratios (Ca/Si > 1.7) is more of an amorphous structure displaying isotropic mechanical properties. Pellenq et al. [52], who developed a molecular structure of C-S-H to achieve a Ca/Si value of about 1.7, also affirmed that the Ca/Si ratio of the C-S-H gel formed generally varies based on the water to cement ratio. This value is expected to be close to 1.0 for general UHPC. Hence, taking this into account, for UHPC, the choice for the simulation rests between jennite with Ca/Si ratio of 1.5 and tobermorite 14 Å with Ca/Si ratio of 0.83.

In addition to the C-S-H, small amounts of portlandite (CH) crystals and ettringite might be present in the microstructure. Therefore, for this study MD simulation was conducted on jennite, tobermorite 14 Å, CH and ettringite, and details of the MD

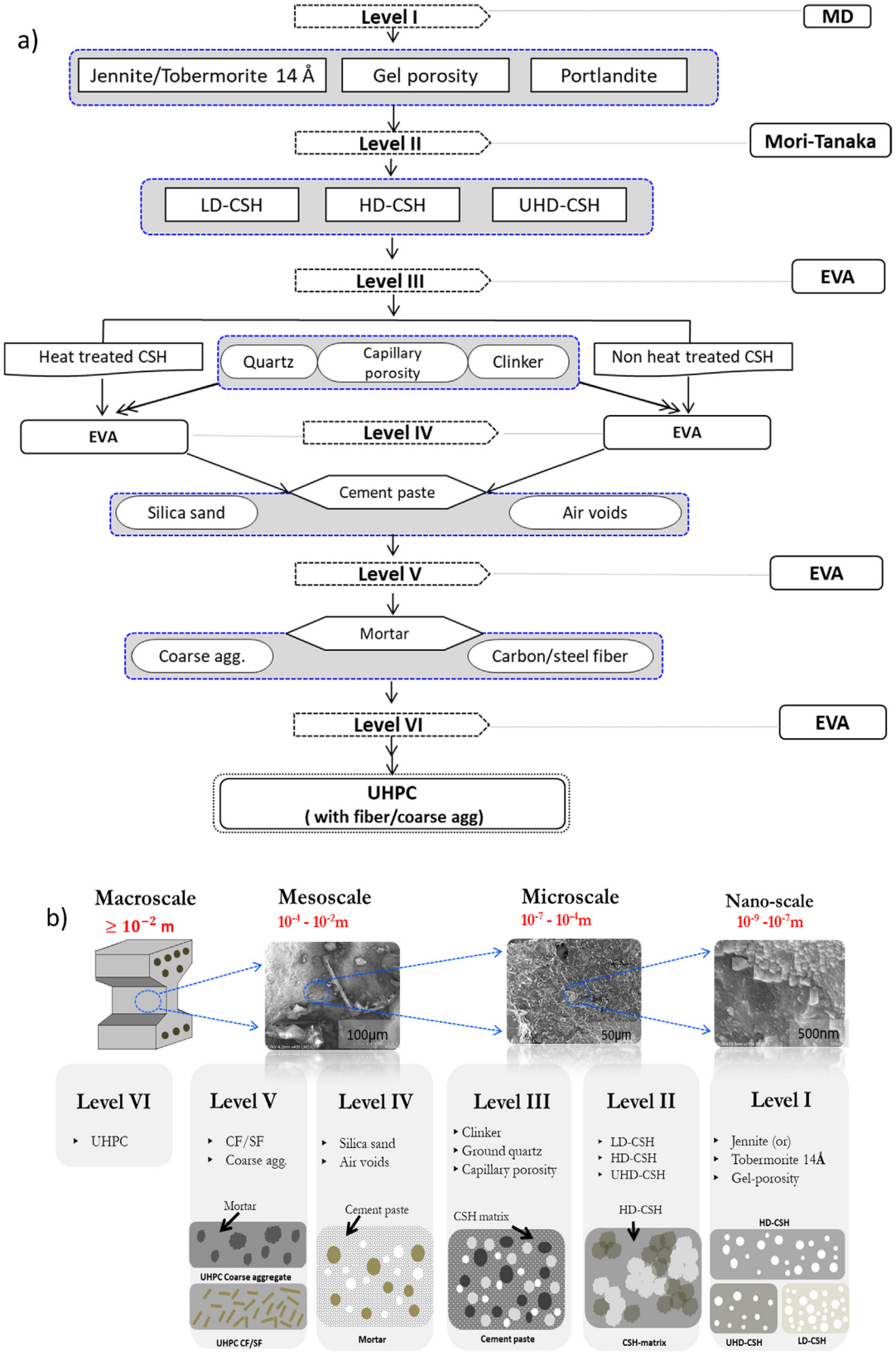

Fig. 1. a) Flow diagram of the multi-level homogenization scheme developed for UHPC b) Schematic representation of the multilevel homogenization.

simulation can be found in Appendix A. After using the MD on the anisotropic crystals, to obtain the elastic moduli of the isotropic polycrysataline CSH, the Voigt-Reuss-Hill approximation [49] is adopted to get the final values.

At Level II, after obtaining the isotropic polycrystalline elastic moduli of the hydration products, the simulation utilizes the micromechanics based Mori-Tanaka model [46] to determine the effective mechanical properties of low density calcium-silicate-

hydrate (LD-CSH), high density (HD-CSH) and ultra-high density CSH, (UHD-CSH) composites. These are made up of the hydration product crystals with varying levels of porosity, whereby the LD-CSH has the highest degree of porosity, while HD-CSH has the medium level and UHD-CSH has very small porosity [53]. The Mori-Tanaka method which gives reasonable estimation of the elastic properties of high concentration composites, utilizes the principles of the representative volume element (RVE) and Eshelby's inclusion principle to determine the effective bulk modulus $(\overline{K})$ and effective shear modulus $(\overline{\mu})$ [54]. This model is applied at this level for its relative computational ease and good levels of accuracy.

At Level III and IV, the ensemble volume averaging (EVA) micromechanical model proposed by Ju and Chen [47] is utilized to determine the effective mechanical properties of the general CSH matrix that will host the different inclusions in the larger length scale and the cement paste matrix. The EVA has the capacity to incorporate the effect of multiple types of inclusions in the matrix, which makes it especially useful for this stage of the analysis. At Level III, two types of CSH matrices are computed, where one is for heat treated UHPC (cured at temperature above 90 °C) and the other for non-heat treated UHPC (cured at normal room temperature). According to literature, based on the heat treatment, the matrix phase and the volume fraction of the inclusion phases will vary [53]. At level III, for UHPC without heat treatment, HD-CSH will be the matrix while LD-CSH and UHD-CSH act as the inclusions. On the other hand, for heat treated UHPC, UHD-CSH will be the dominant phase hence the inclusions will be the LD-CSH and HD-CSH. At level IV, the matrix phase is assumed to be the general CSH matrix and the inclusions while the ground quartz, capillary porosity and the clinker will be taken as the inclusions. Details of the computations will be discussed in section 4.

According to the EVA method for non-interacting, unidirectionally aligned, and similar shaped inclusions, the effective stiffness tensor represented by $\mathbf{C}^*$ is given as follows [47,54]

$$\mathbf{C}^* = \mathbf{C}_0\left\{\mathbf{I} + \sum_{r=1}^{2}\left[\phi_r(\mathbf{A}_r + \mathbf{S}_r)^{-1}\cdot\left\{\mathbf{I} - \phi_r\mathbf{S}_r\cdot(\mathbf{A}_r + \mathbf{S}_r)^{-1}\right\}^{-1}\right]\right\} \quad (1)$$

where $\mathbf{C}_0$, $\mathbf{I}$, ϕ_r, $\mathbf{S}_r$, and $\mathbf{A}_r$ are the stiffness tensor for the matrix phase, the fourth-order identity tensor, the volume fraction of the r-phase inclusion, Eshelby's tensor for the r-phase inclusion, and the strain concentration tensor, respectively [47,54]. For this study, two different types of inclusion shapes are considered: spherical shape for the hydration products, fine sand, aggregates, air voids; and prolate spheroidal shape for the carbon fiber (CF) and steel fiber (SF) inclusions. The general forms of the Eshelby's tensor for the spherical and prolate spheroidal inclusions can be found in [55]. In addition, all the inclusions are initially modeled assuming they have a perfect interface condition. Appendix B shows the components of Eq. (1).

In a similar manner, at Levels V and VI, the EVA micromechanical model is utilized to determine the effective elastic properties. From the homogenization of Level V, the mortar phase is obtained, which is composed of the cement paste as the matrix phase and the silica sand and air voids (entrapped air) as inclusions. Next, for Level VI homogenization, the final fiber reinforced UHPC is obtained where the mortar of level V acts as the matrix and the carbon fiber (CF), steel fiber (SF) and coarse aggregates act as inclusions. However for the simulation, the CF, SF and coarse aggregates are each embedded in the mortar matrix separately, which means the final UHPC composite doesn't contain all three of them together.

The EVA model is applied to determine the UHPC with CF and SF. In this model, since the orientation of fibers in the final UHPC phase can be either randomly oriented or aligned in the same direction, a 3D orientational averaging process is applied on the effective stiffness tensor to determine the elastic properties for randomly oriented fiber inclusions [43–45,56,57]. For this study, the approach proposed by Lee and Simunovic [58] is adopted in which the effective stiffness tensor after the 3D orientational averaging process becomes [42,45]

$$\mathbf{C}^* = \widehat{C}^{(1)}_{IK}\delta_{ij}\delta_{kl} + \widehat{C}^{(2)}_{IJ}\left(\delta_{ik}\delta_{jl} + \delta_{il}\delta_{jk}\right) \quad (2)$$

where the components of the tensors $\widehat{C}^{(1)}_{IK}$ and $\widehat{C}^{(2)}_{IJ}$ are functions of $C^{(1)}_{IJ}$ and $C^{(2)}_{IK}$ from Eq. (1) and whose components can be found in [55]. Here, it is important to note that the hat indicates the values after the orientational averaging process.

In Level VI, in order to model the coarse aggregates as inclusions in the UHPC mortar matrix, a form of composite sphere micromechanical model is adopted. In the composite sphere model, the material is modeled as an effective medium that has spherical inclusions of certain radius, with outer shells of a given radius [48]. This study adopted the four-phase composite sphere model developed by Li et al. [32], which adds an additional intermediate shell between the particle and the matrix material to account for the interfacial transition zone (ITZ), which can be seen in Fig. 2. This modification makes it especially suited to model cementitious composites such as concrete. Using this tool, the effective bulk modulus $(\overline{K})$ is obtained. And finally, the rule of mixtures is utilized to determine the effective Poisson's ratio (υ_{eff}). The details of this computation can be found in [32].

Finally, at Level VI again, since an important factor that determines the effectiveness of fibers in UHPC is the bond or interface condition between the inclusion and the matrix phase, this study adopted an interface modeling scheme proposed by Qu [59], that defines an imperfect interface as having a discontinuous displacement field across the interface. According to this method, the interface is modeled as a linear spring-layer of vanishing thickness, which is characterized by a second-order tensor (η_{ij}) known as the compliance tensor [59]. Using the compliance parameter η_{ij}, the value of the modified Eshelby's tensor (S^M_{ijkl}) can be computed from the original perfectly bonded Eshelby's tensor S_{ijkl}. The compliance tensor is given by [48,59]

$$\eta_{ij} = \alpha\delta_{ij} + (\beta - \alpha)n_i n_j \quad (3)$$

where α and β represent the compliance in the tangential and normal direction, respectively; n_i represent the unit outward normal vector, and $\delta_{ij}$is the Kronecker's delta [59]. In this model, the values of α and β would be zero at a perfectly bonded interface, whereas, at a completely debonded interface, the values of α and β would approach ∞ [59]. The modified Eshelby's tensor for spheroidal inclusion is given by [55]

$$(S_{n+1})^M_{ijkl} = \frac{1}{4(1-\upsilon_0)}\left[S^{M(2n-1)}_{IK}\delta_{ij}\delta_{kl} + S^{M(2n)}_{IJ}\left(\delta_{ik}\delta_{jl} + \delta_{il}\delta_{jk}\right)\right] \quad (4)$$

where n = 1 or 2 indicates mild and severe imperfect interface conditions, respectively. The second-order tensors $S^{M(2n-1)}_{IK}$ and $S^{M(2n)}_{IJ}$, which are functions of the compliance tensor η_{ij} and Eshelby's tensor components S_{IJ} andS_{KL} of the original spheroidal inclusions, are given in Pyo and Lee [55].

3. Microstructure of UHPC at different levels

An experimental investigation consisting of compressive strength tests, SEM and MIP analysis was conducted on three types of UHPC samples in order to qualitatively determine the phases present, observe porosity and interface conditions and finally vali-

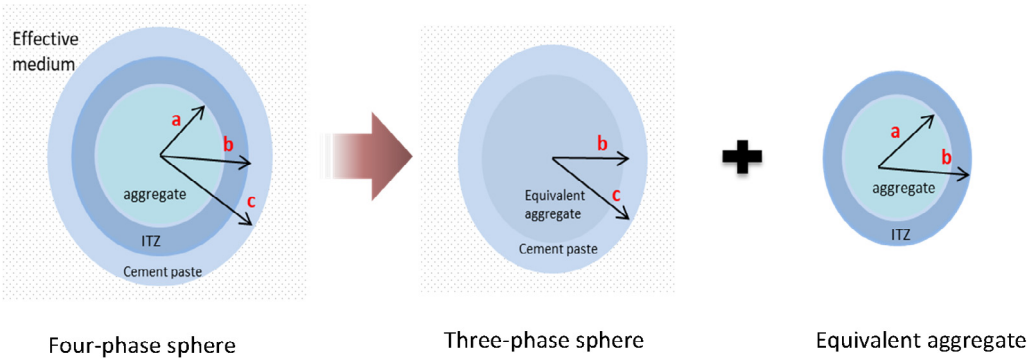

Fig. 2. Schematics of composite sphere model.

date the model output. Cubic samples of size 5 cm were prepared and cured for 28 days in a water bath at 90 °C before testing. In addition, literature was referred to confirm the observations and obtain parameters such as porosity levels in the hydration products like the LD and HD CSH.

Three types of UHPC mixtures with different proportions of CF, SF, and coarse aggregates were prepared by varying the parameters of the inclusions such as the volume fraction for CF and SF and weight percent for the coarse aggregates. Table 1 shows the mix proportions prepared for this study. The constituents of UHPC include cementitious components, such as Portland cement and the pozzolanic materials silica fume and nano-silica, fillers with different length scales such as ground quartz, and silica sand, and finally the different fiber inclusions that are added to improve the ductility and the compressive and tensile strengths. Since UHPC requires high-density packing, the combined particle size distribution of all constituents should be well graded. The particle size range and distribution of the constituents that were used are for nano silica (0.01–0.05 μm), silica fume (0.1–0.2 μm), ground quartz (10–15 μm), cement (10–80 μm), fine sand (10–600 μm), and coarse aggregates with varying maximum aggregate size of 5.0 mm to 50.0 mm.

After the curing of the samples, the microstructure of the material was studied with the help of SEM and MIP to verify the modeling assumptions regarding the volume fraction, porosity, existence of micro-cracks, and condition of the interface. The analysis of the SEM images was conducted to qualitatively determine the phases present at the different length scales of the simulation. Fig. 3 shows the SEM images, while Fig. 4 shows the MIP results.

As can be observed from the subfigures in Fig. 3, which are at different magnifications, the hydration product that was mainly observed was CSH, while almost negligible amounts of CH and ettringite were observed. On the other hand, a large amount of unreacted clinker and quartz powder was observed; see Fig. 3(b) and (c). In Fig. 3(e) and (f), the samples with a coarse aggregate appear to be more porous than the other UHPC samples. Fig. 3(f) shows the existence of a very thin ITZ around the coarse aggregates, while Fig. 3(a) shows the fine aggregates as having almost no visible ITZ. Lastly, in Fig. 3(g) and (h), it can be observed that the SF has a very rough surface at the microscale, which facilitates adherence of the CSH gel. On the other hand, the CFs, which are much smaller, have a rather smooth and slippery surface that discourages effective bonding between the fiber and the CSH gel. Hence, the interface between the CFs and the surrounding CSH matrix is expected to be weaker.

The hydration products of cement are generally porous with the pore structure having various shapes and sizes [49,50]. When multi-level modeling of UHPC is conducted, it is important to explore the pore structure and determine the nature of the pores that exist and at which length scale they exist in the cementitious composite. Pores in cementitious composites have been classified into the following four groups: gel pores, capillary pores, entrained air, and entrapped air [51,52]. Gel pores are generally considered as intrinsic parts of the amorphous CSH gel [60]. The MIP results provide a rough indication of the presence of these gel pores and capillary pores. Capillary pores depend on the water to cement ratio and hydration age [61]; thus, UHPC contains a relatively small number of these pores.

Fig. 4 shows that the samples with CF (UHPC 2-1) appeared to have the largest porosity. This observation indicates that the inclusion of CFs in UHPC increases the porosity owing to their interface slipping property. This observation is also in line with the observa-

Table 1
Proportions of UHPC mixtures in (wt%).

Materials	UHPC 1–1 Control	UHPC 2–1 (CF)	UHPC 2–2 (SF)	UHPC 3–1 (4.75 mm)**	UHPC 3–2 (9.5 mm)**
Cement	1	1	1	1	1
Silica fume	0.25	0.25	0.25	0.25	0.25
Nano-silica	0.02	0.02	0.02	0.02	0.02
Ground quartz	0.35	0.35	0.35	–	–
Silica sand	1.1	1.1	1.1	1.1	1.1
Coarse aggregate	–	–	–	0.60	0.60
Water	0.23	0.23	0.23	0.22	0.22
Superplasticizer	0.04	0.04	0.04	0.04	0.04
Steel fiber*	–	–	2	–	–
Carbon fiber*	–	2	–	–	–

*In volume fraction (%).
**Maximum aggregate size (r_{max}).

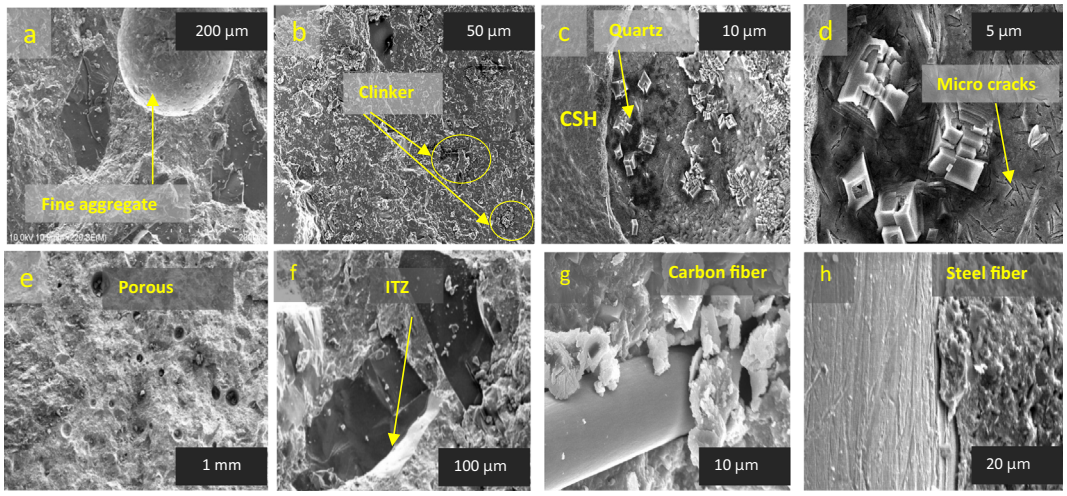

Fig. 3. SEM images for the prepared UHPC samples: (a-d) basic constituents and hydration products; (e, f) effects of adding coarse aggregates; (g, h) difference in surface properties between carbon fiber and steel fiber in UHPC.

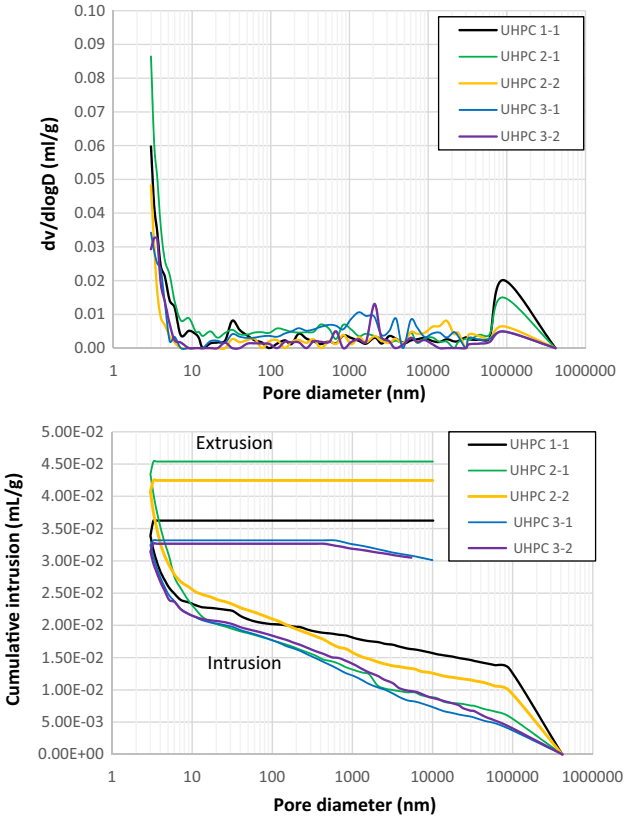

Fig. 4. Pore size distributions of specimens with carbon and steel fiber (UHPC 1–1 (Control), UHPC 2–1 (2% CF), UHPC 2–2 (2% SF), UHPC 3–1 (60% of r_{max} = 4.75 mm coarse aggregate), UHP C 3–2 (60% of r_{max} = 9.50 mm coarse aggregate).

tions of the fiber interfaces from our SEM analysis and results in the literature that suggest that fibers generally increase the porosity of UHPC in the hardened state [62].

In addition, the analysis of the cumulative volume intrusion curve of the MIP test enables us to determine in which range most of the porosity exists. This is accomplished first by taking the total volumes intruded in the specific pore size ranges, then determining the percentage of that volume from the total intruded mercury volume. This computation is given in Table 2. The calculation determined that, for the prepared control mix, the UHPC 1-1 total porosity from the MIP test was 7.40% and the gel porosity, capillary porosity, and entrapped air were obtained to be 2.35%, 2.03%, and 3.02%, respectively.

4. Simulation results at different levels

4.1. Level I: Molecular dynamics simulation results

The homogenization process and results at each level of the material are discussed subsequently. For concrete at the nanoscale level, we find the highly gel-like amorphous C-S-H, which exists with variable structures based on the chemical molar ratio of the Ca/Si, which ranges from 0.7 to 1.6 [63,64]. Even though the actual molecular structure of CSH has not been fully understood yet, due to its close proximity to the structures of tobermorite 14 Å and jennite molecular dynamics based studies have focused on modeling it as one of these crystal materials [65,66]. Therefore, the MD simulation was conducted on these two structures and the values obtained for the Young's modulus and Poisson's ratio were 71.39 GPa and 0.38 for jennite, and 91.62 GPa and 0.28 for tobermorite 14 Å, respectively. In this study, the MD was conducted on both jennite and tobermorite 14 Å as we wanted to investigate the difference in their elastic properties (Young's modulus and Poisson's ratio). But from the MD simulation, for tobermorite 14 Å, the Young's modules value obtained was too large as compared to values presented in literature for the general C-S-H matrix from nano-indentation experiments. For the second level homogenization, since jennite or tobermorite 14 Å are supposed to be the building blocks for the C-S-H matrix, the MD results suggested that the C-S-H structure has closer elastic properties to jennite. Hence, for this study, the subsequent homogenizations were conducted using jennite.

In addition, as the other hydration product that can be present in UHPC is portlandite (CH), MD simulation of the CH molecule provided an elastic modulus of 55.74 GPa and 0.40 for Poisson's ratio. The values obtained by the MD simulation are reasonable when compared to values from literature using nano-indentation and other MD simulations [50,51]. These values are used as input parameters for the homogenization of the hydration products with gel porosity to form the different kinds of CSH.

4.2. Level II: Micromechanics of LD, HD, and UHD-CSH

At the second level of homogenization, the main hydration products are homogenized into a single matrix phase that essen-

Table 2
Calculation of porosity distribution in the different length scales from MIP test.

	UHPC 1–1		UHPC 2–1		UHPC 2–2		UHPC 3–1		UHPC 3–2	
Total porosity (%)	7.40		10.50		4.72		6.27		3.90	
Average pore diameter (nm)	12.60		8.66		13.70		16.30		8.10	
	V (%)	P (%)	V (%)	P (%)	V (%)	P (%)	V (%)	P (%)	V (%)	P (%)
Gel porosity (0.5–10 nm)	31.74	2.35	63	5.45	21	0.99	30	1.88	67	2.61
Capillary porosity (10–10,000 nm)	27.43	2.03	29	2.51	27	1.27	49	3.07	28	1.09
Entrapped air (50–1250 μm)	40.82	3.02	8	0.69	52	2.45	10	0.63	5	0.19
Total	100	7.4	100	8.66	100	4.73	100	6.27	100	3.9

V (%): Percentage of total mercury volume intruded.
P (%): Percentage from total porosity.

tially hosts all the other inclusions in the higher length scales. CSH gel is a very porous phase with large portions of gel pores of sizes ranging from 0.5 to 10 nm. These gel pores might be filled with water or air, but for this study the gel pores are assumed as spherical shaped inclusions with negligible Young's modulus and Poisson's ratio.

Previous studies have shown that based on the location and the hydration conditions, the CSH-gel exists in two or three general forms [52] i.e., low-density (LD), high-density (HD), and ultra-high-density (UHD) CSH. These three phases are chemically similar and show a slight dependence only on the water to cement ratio [53]. According to previous works by Vandamme et al. [53], gel porosity is considered as an intrinsic part of the LD and HD-CSH matrices, which implies that based on the packing density and the molecular structure of the materials, we can determine the porosity which is also referred to as the gel porosity. Recent works based on NMR relaxometry and analytical analysis on the densification of C-S-H [38,39], showed that based on the degree of hydration and w/c ratio, the precipitating CSH-gel can have variable densities depending on the quantity called specific precipitation space. According to these studies, based on the hydration regime, two classes of CSH form. Class A CSH, which forms at the initial stages of hydration, is a CSH that is dense, ordered and without gel pores as it precipitates, while, Class B CSH precipitates in the open spaces of capillary porosities and gel porosity. For this class, because the precipitation space is available, the CSH formed is less dense and with a large amount of gel porosity. This classification actually reinforces the assumption of the existence of hydration products with different densities, which is similar to the previous classification of LD, HD (Class B CSH) and UHD-CSH (Class A CSH). In this study the LD, HD and UHD classification was adopted due to its simplicity and as it is easier to find literature values for validation of the model results.

"The current developed multi-level homogenization scheme assumes a fixed hydration degree of 60%, which is the expected degree of hydration for UHPC at the age of 28 days. Hence, the density of CSH as it evolves with increased hydration and hydration modeling will be out of the scope of this study. In addition, by representing CSH as LD-CSH, HD-SH and UHD-CSH, which have variable porosities based on the w/c ratio, the location of precipitation, the hydration degree and the hydration condition, we are effectively representing the CSH general matrix as a composite made up of inclusions having different densities.

Consequently, for the study the gel porosity amounts for LD-CSH, HD-CSH and UHD-CSH were obtained from literature suggested values of the particle packing model. On the basis of nano-indentation techniques, several researchers showed that the packing density of LD-CSH and HD-CSH globules is approximately 63% and 76%, respectively; hence, the gel-porosity becomes 37% and 24%, respectively [52–54,59]. Finally the third phase, UHD-CSH, is much less porous than HD-CSH with particle packing density of approximately 83% and gel porosity of 17% [53].

The Mori-Tanaka method is adopted in the current study to homogenize the composites as it is highly effective for high and low concentrations of inclusions. In addition, for the special case when the inclusions are voids, the Mori-Tanaka method provides better solutions [46]. At this level of the study, the LD-CSH and HD-CSH properties were computed by assuming the hydration products resemble jennite crystals considering Ca/Si ratio to be more than one. The jennite will act as the matrix phase in which the porosity will be modeled as spherical inclusions, with zero stiffness and Poisson's ratio, embedded in the continuous matrix. Furthermore, according to microstructural investigations of concrete consisting of a low water-to-cement ratio, UHD-CSH is a nanocomposite of HD-CSH and CH [53]. Hence, UHD-CSH was obtained by homogenizing these two forms into a single matrix phase. Table 3 provides the modeling parameters and summary of the results of the homogenization conducted at Level II along with a comparison with the values in the literature. The values from literature were obtained using nano-indentation techniques and micromechanical modeling techniques such as self-consistent method and Mori-Tanaka method. From the values, it

Table 3
Level II Mori-Tanaka simulation results.

Predicted phases	Input phase	Volume fraction (%) [36,53]	Prediction results		Literature
			E (GPa)	υ	E (GPa)
LD-CSH	Jennite	63	32.98	0.32	22.5[a], 25[b] 30.8[d], 39[c]
	porosity	37			
HD-CSH	Jennite	76	43.87	0.34	41[b,d], 30.4[a], 48.6[c]
	porosity	24			
UHD-CSH	HD-CSH	80	46.02	0.35	40.9[a]
	CH	20			

a : Literature value from nano-indentation by Vandamme et al. [53].
b : Literature values from Mori-Tanaka micromechanics homogenization by Hajilar et al. [49].
c : Literature values from self-consistent micromechanics homogenization by Hajilar et al. [49].
d : Literature values from Microporomechanics homogenization by A. Al-Ostaz et al. [35].

can be seen that our simulation results lay within the range of reported values, with the experimental results presenting the lower thresholds. The micromechanical modeling techniques present higher values as they assume perfect and ideal microstructures that do not consider internal defects. This presents marginal deviation from the experimental results. For the next level of homogenization, the CSH properties obtained will be used as input parameters. As mentioned in section 2, the values given in Table 3 for jennite are isotropic because the Voigt-Reuss-Hill approximation [49] has been applied on the MD values of the anisotropic crystals, to obtain the elastic moduli of the isotropic and amorphous polycrysataline CSH.

4.3. Level III: Micromechanics of CSH matrix

The LD-CSH, HD-CSH, and UHD-CSH are homogenized into an effective material that can be assumed to be isotropic and homogeneous at this scale. This phase is generally known as the CSH matrix phase, and serves as the medium in which other inclusions are to be embedded. For a concrete mix with a water to cement ratio of approximately 0.2, based on the curing conditions or heat treatment, one of the two densely packed hydration products form the more abundant phase [53,67,68]. When the mixture is heat cured at 90 °C, the UHD-CSH phase forms more dominantly, whereas the LD-CSH and HD-CSH form in almost equal amounts [53].

Hence, this study adopts the EVA micromechanics method by considering the system as a three-phase composite and the two inclusions as spherical inclusions with perfect interface conditions. In the absence of heat treatment, HD-CSH is considered as the matrix phase; otherwise, UHD-CSH serves as the matrix. Table 4 lists the simulation conditions and the results of the two types of CSH matrices formed. In this table the proportions of the three CSH phases is adopted from Vandamme et al.'s [53] experimental work on low w/c ratio concrete. After the simulation, the result indicates that both the heat-treated and non-heat-treated CSH matrix have almost similar mechanical properties. This observation agrees well with experimental predictions in the literature, which suggest that heat treatment at or below 90 °C has minimal effect on increasing the compressive strength or the Young's modulus of UHPC [55,69].

4.4. Level IV: Micromechanics of cement paste

At this level of homogenization, the simulation assumes three types of spherical inclusions embedded in the CSH matrix, i.e., the capillary porosity, unreactive quartz, and unreacted cement clinker, which occurs as a result of the low water to cement ratio (0.2) and hydration degree of only 60% [70,71]. The smallest inclusions are the capillary pores whereas the largest particles are the unreacted cement clinkers.

The predictions obtained with our model were verified experimentally by using SEM for qualitative verification of the phases present, after which the MIP results were analyzed to determine the total porosity, gel porosity, capillary porosity, and entrapped air volume fractions. Table 2 shows the computation of porosities from the MIP test. In addition, the prepared mix design was used to calculate the volume fractions of the quartz and unreacted clinker. The volumes of the three inclusions are then determined by considering that quartz is an unreactive phase; hence its volume remains unchanged and the cement clinker as 40% of the original cement volume fraction of the total mix.

The general mix design is used to determine the volume fraction of each constituent by using their specific gravity. Subsequently, the volume fraction of the phases that are present at this homogenization level is extracted and recalculated to obtain the new volume fractions. The initial volume fractions of the phases are approximately 12.49% and 39.26% for quartz and fine sand, respectively. Then the capillary porosity from the MIP analysis and volume of added fibers form 2.03% and 2.00% by volume of the total mix, respectively. Using these values, Table 5 demonstrates the recalculation of the new volume fraction of the CSH matrix containing only the quartz, cement clinker and capillary porosity. Note that during hydration, the volume of the general material is reduced because of the thermodynamic reaction and hence the total volume fraction of the products cannot be expected to be 100%, as some phases disappear and new phases form [72]. However, since the thermodynamic analysis is not in the scope of this work, we only focus on the unreacted phases which remain constant in the material, such as the ground quartz and cement clinker which is 40% of the initial cement content, since the expected hydration rate is approximately 60% [70].

Using the above assumptions and computations, the final phases of inclusions at this level of homogenization are summarized in Table 6. The results of the analysis indicate that, even though the input parameters are different, the effective mechanical properties of the cement paste are very close. This is mainly due to the mechanical properties of the CSH matrix phase and the ground quartz, for which the values of Young's modulus are similar. From the Level IV homogenization, we also note the reinforcing effect of the unreacted clinker, which is by volume calculated as being 40%

Table 5
Computation of volume fractions (%) for the quartz powder and cement clinker.

Volume fractions at homogenization level IV (%)				
Component		Total	Extraction	Recalculation
CSH	x	31.50	31.50	53.76
Quartz powder	12.49	12.49	12.49	21.31
Capillary porosity	2.03	2.03	2.03	3.41
Clinker	0.4 x	12.60	12.60	21.50
Steel fiber	2	2.00	–	–
Fine sand	39	39.00	–	–
	100		59	

x: indicates the volume fraction of hydration products (CSH) to be calculated by assuming total volume is 100%. Note the CSH will constitute all the phases that reacted to give the hydration products. Note that this computation is not thermodynamically conducted, and is a rough estimate to determine the unreacted phases.

Table 4
Level III input parameters and EVA homogenization results (CSH-matrix).

Method	Output	Component	V (%) [53]	Input parameters		Simulation Results	
				E (GPa)	υ	E (GPa)	υ
Ensemble volume averaging	CSH- no heat treatment	LD-CSH	3	32.95	0.32	43.98	0.34
		HD-CSH	74	43.87	0.34		
		UHD-CSH	23	46.02	0.35		
	CSH-heat treatment	LD-CSH	13	32.95	0.32	43.81	0.34
		HD-CSH	13	43.87	0.34		
		UHD-CSH	74	46.02	0.35		

Table 6
Level IV EVA homogenization results (cement paste).

prediction	Component	Volume fraction (%)	Particle size	Input parameters		Simulation results	
				E (GPa)	υ	E (GPa)	υ
Cement paste	CSH	53.80	matrix	43.98	0.34	52.05	0.30
	Ground quartz	21.31	10–15 μ m	48.20	0.20		
	Capillary porosity	3.41	0.01–50 μ m	–	–		
	Clinker	21.50	10–80 μ m	128.40	0.30		

of the initial volume content of the Portland cement. Most of the significant increase in the modulus we observe at this level is mainly attributable to this unreacted clinker.

4.5. Level V: Micromechanics of UHPC mortar

In order to conduct the homogenization at this level, whereby the inclusions in the cement paste are silica sand and air voids with sizes ranging from 10 μm to 1.2 mm, the volume fractions of the silica sand and the air voids (entrapped and entrained air) should be determined. This can be achieved by applying a similar computation as for level IV, in which 39.5% of the 100% UHPC mortar phase is silica sand and 3.04% consists of air voids. This means the matrix phase, cement paste, constitutes 57.46%. Subsequently, the EVA micromechanical method can be used to compute the effective mechanical properties of the cement paste phase. In addition, the qualitative image analysis Fig. 3(a), shows no significant amount of ITZ between the sand particles and cement paste; hence, perfect interface conditions are assumed. The input parameters and the output from the micromechanical simulation are presented in Table 7.

4.6. Level VI: Micromechanics of UHPC with fibers and aggregates

(1) Homogenization of CF and SF

In Level VI, the homogenization is conducted by using the EVA micromechanical model whereby the inclusions are CF and SF with different aspect ratios. The fiber inclusions are assumed to have prolate spheroidal shapes, and both perfect and mildly weakened interfaces are considered in this study. Table 8 presents the input parameters utilized for the simulation and the predicted results for UHPC with randomly oriented CF and SF. The results show that the increase in Young's is only approximately 3% when 2% of CF and SF are added. This observation agrees well with literature predictions [73–76].

(2) Homogenization of coarse aggregates in UHPC

The results in literature suggest that adding coarse aggregates to UHPC tends to reduce the strength of concrete mainly due to the formation of weak zones in the form of ITZs [31,61]. In this study, the optimal size range and volume fraction of coarse aggregate are computed in addition to analyzing the influence of the ITZ zone by considering different Young's moduli and the thickness of the ITZ layer around the coarse aggregates.

The four-phase composite sphere model described in Section 2.4 is utilized to compute the effective properties of the UHPC with coarse aggregates. Since the model depends on the particle size distribution of the coarse aggregates to determine the volume fraction of the ITZ and cement paste, the calculation is performed by using the method known as Modified Fuller's particles size distribution [32]. Using this method, we investigated the effect of the aggregate size by considering different particle size groups that have maximum radii of 2.4, 5.0, 9.5, 15.3, 25.0, 37.5, and 50.0 mm.

Fig. 5 shows the effect of adding coarse aggregate with a maximum radius of 5.0, 9.5, and 50 mm. The simulation is conducted using the four-phase composite sphere model, and as can be observed, initially the modulus increases until the aggregate volume reaches approximately 25%, then it decreases with further increases in the volume fraction of the coarse aggregates. The analysis was conducted by assuming a constant ITZ thickness of 50 μm, and ITZ Young's modulus of 80% of the Young's modulus of the UHPC mortar [32]. These results show that, even though a constant thickness of ITZ is assumed, an increase in the volume fraction of

Table 7
Level V EVA homogenization results (UHPC mortar).

Prediction	Component	Volume fraction (%)	Particle size	Input parameters		Simulation results	
				E (GPa)	υ	E (GPa)	υ
UHPC mortar	Cement paste	57.46	matrix	52.05	0.30	56.18	0.26
	Silica sand	39.50	10–600μ m	73.20	0.20		
	Air voids*	3.04	50–1250μ m	–	–		

Air voids*: is the total of entrapped and entrained porosity in the composite

Table 8
Micromechanics based analysis of UHPC with fibers and coarse aggregates.

	Component	Volume fraction (%)	Aspect ratio	Particle size	Input parameters		Predicted results
					E (GPa)	υ	E (GPa)
	UHPC mortar	(98, 60, 40)*	–	–	56.18	0.26	
UHPC with fibers	Carbon fiber	2	3000	5–7 μm by 15 mm	240	0.20	58.28
	Steel fiber	2	65	0.2 mm by 13 mm	200	0.30	57.94
UHPC with aggregate	Coarse aggregate (Basalt) [70]	60*	–	0.15-r_{max}** mm (varies)	54	0.15	–
	ITZ [33]	5–7*	–	t = 50 μm	(0.6–0.8) of E_{mortar}	0.30	–

*the volume fraction is variable and depends on the aggregate size distribution and assumed ITZ thickness.
**r_{max} can be taken as 2.4, 5.0, 9.5, 25.0, 37.5, and 50.0 mm.

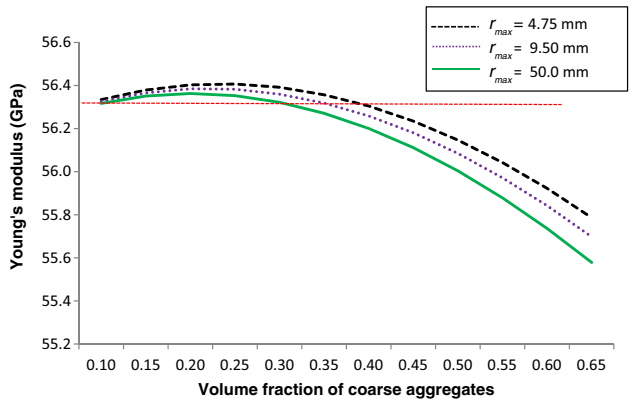

Fig. 5. Young's modulus (E_{eff}) as a function of the volume fraction of coarse aggregates with a maximum size of 5.0 mm, 9.5 mm and 50.0 mm in UHPC samples.

the coarse aggregates leads to a gradual decrease in the Young's modulus. These results are in good agreement with the prediction from literature [77,78]. The figure also indicates that larger coarse aggregates tend to reduce the effective properties more than the smaller aggregates.

4.7. Multi-level homogenization results

As it is progressed through the multi-level homogenization scheme, the change in the mechanical properties of the material at the different length scales can be observed. With each homogenization, certain properties become magnified, whereas others are averaged. Fig. 6 shows the change in the Young's modulus (E) and Poisson's ratio (v) at each microstructural level of the analysis. The figure also helps for the purpose of designing a mix with optimized properties, by taking into account the effects of each constituent. The figure presents the comparison of the Young's modulus and Poisson's ratio from each homogenization level.

5. Model verification

According to literature, based on fiber content and aggregates content, the Young's modules of UHPC can range between 45 and 70 GPa [5]. For this work, based on the mix design presented in Table 1 and the curing condition discussed, the Young's modulus (E_c) was empirically computed from the experimentally determined compressive strengths (f_c) to compare the experimental values with the model predictions. Note that the developed model's Young's modulus prediction is independent of specimen shape or dimension due to the RVE and the micromechanical modeling's assumptions; hence, comparison with the experimental correlated values is possible. For the comparison, empirical equations developed for high strength concrete by several researchers and different design codes were adopt. These include equations from Ma et al. [77] for UHPC with coarse aggregates, CEB-FIP [79] and Eurocode 2004 [80], ACI committee 363 [81] and finally Noguchi et al. [82], which are presented in Table 9. These were specifically selected as they were suitable to correlate the Young's modulus of concrete with high strength compressive strength values.

Fig. 7 shows the comparison of the experimental and the model predicted values of the Young's modulus of the control UHPC sample and the samples with 2% CF and 2% SF. From the comparison, it can be concluded that our modeling results provide higher values of the Young's modulus as compared to the other empirical equations. On average, the values tend to show variations in the range of 5% to 15%, and the highest deviation was observed for UHPC with CF. The possible causes of the deviation are the initial high moduli obtained for the hydration products of jennite and CSH, and the fact that the multi-level homogenization assumes the level of hydration as approximately 60% and the presence and disappearance of certain phases, which might vary from the experimental condition. In addition, other sources of error can be due to the comparison being made with Young's modulus values obtained from the adopted empirical equations, which do not consider additional inclusion in the samples (e.g., CF).

The model predictions for the case of UHPC with coarse aggregates were verified by comparing with the experimental compressive strength results available from the literature (Esteban et al. [83], (UHPC CA-1), and Ma et al. [77], (UHPC CA-2)) which employed mix designs that closely resembled the mix designed used for the multilevel homogenization that is used in this study. Hence, the matrix phase for this micromechanical analysis will have similar mechanical properties. In addition, the literature provided full information on the coarse aggregates parameters required to conduct the micromechanical analysis. Table 10 shows

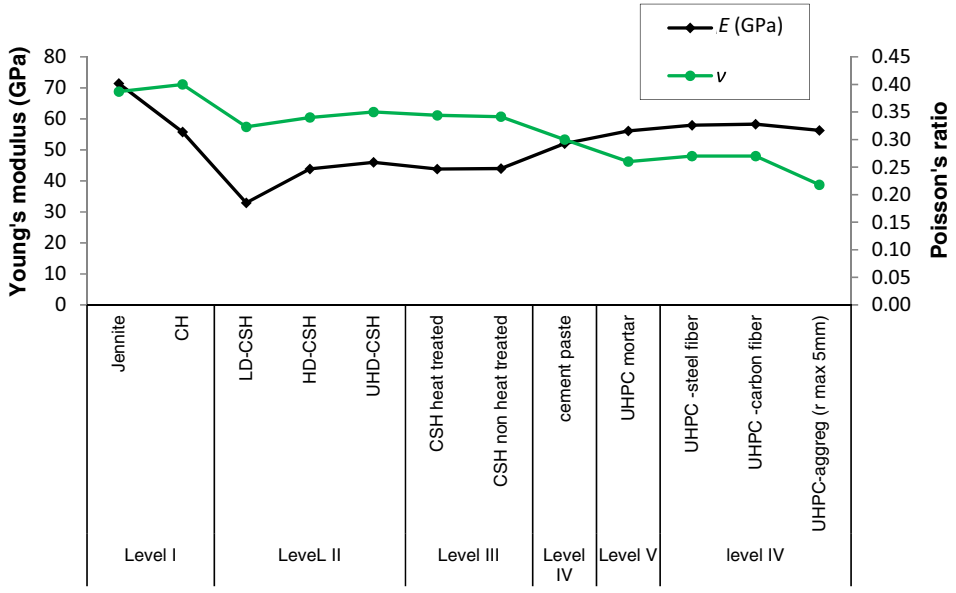

Fig. 6. The results of the multi-level homogenization.

Table 9
Empirical equations used to relate the elastic modulus with compressive strength values.

Model references	Empirical model for UHPC (MPa)
CEB-FIP/Eurocode (2004) [79,80]	$Ec = 22000\left(\frac{f_c}{10}\right)^{1/3}$
Ma et al. [77] (with coarse aggregate)	$Ec = 21902\sqrt[3]{f_c/10}$
ACI committee 363 [81]	$Ec = 21000\left(\frac{\gamma}{2300}\right)^{1.5}\left(\frac{f_c}{20}\right)^{1/2}$
Noguchi et al. [82]	$Ec = 1.146 \times 1.486 \times 10^{-3} f_c^{1/3}\gamma^2$

γ : Unit weight of UHPC, (2500 Kg/m^3).
f_c : Compressive strength of the UHPC.

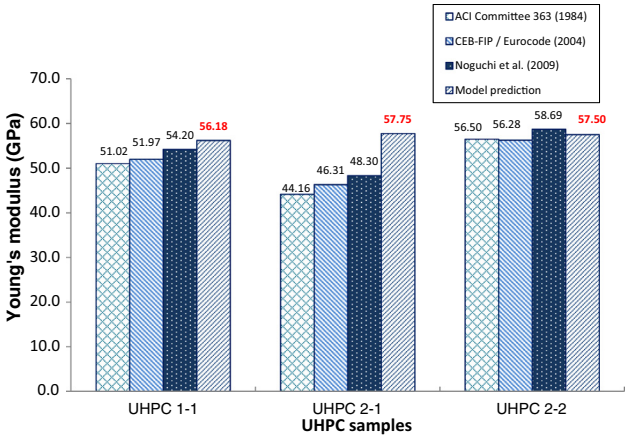

Fig. 7. Comparison of the experimental and the model predicted values of the Young's modulus of UHPC 1–1 (Control), UHPC 2–1 (2% CF) and UHPC 2–2 (2% SF).

the parameters obtained from the literature and used for the simulation of UHPC with coarse aggregates, while Fig. 8 shows the comparison of experimental values from the literature and the model predicted values of the Young's modulus of UHPC with coarse aggregates. The deviation between the experimental values and the model predictions are less than 9% for all three cases. While some deviation in the results is expected from the computation of the Young's modulus from the empirical formula developed by Ma et al. [77], the errors related to the micromechanics method adopted here might be due to the simplifying assumptions that are incorporated, such as the ITZ layers being of constant thickness.

6. Parametric investigation

6.1. Effect of fiber type and orientation

Based on the parameters presented in Table 8, the effects of fiber orientation and fiber type were investigated for different volume fractions of the fibers. The literature suggests that the orientation of the fibers in the structural elements is independent of the type and content of fibers but depends on the method used

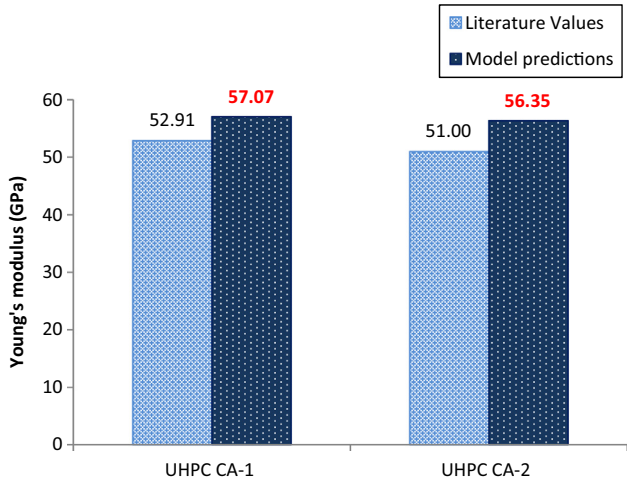

Fig. 8. Comparison of literature experimental values and model predicted values of the Young's modulus of UHPC samples with coarse aggregates, (UHPC CA-1 from Esteban et al. [67], and UHPC CA-2 from Ma et al. [60]).

to pour the concrete, location in the member, and placing direction [13]. In this study, the EVA method for aligned and random distribution of short fibers in composites proposed by Pyo and Lee [55] is adopted to investigate the properties of UHPC with different volume fractions of CF and SF.

Fig. 9 compares the Young's modulus (E) for UHPC composed of CF and SF, where E_L and E_T indicate the Young's modulus in the longitudinal and tangential directions, respectively. Note that for this step, perfect interface conditions are assumed for both types of fibers. Without taking into account the bonding behavior, the CFs out-performs the SF by approximately 1–5%. Furthermore, the per-

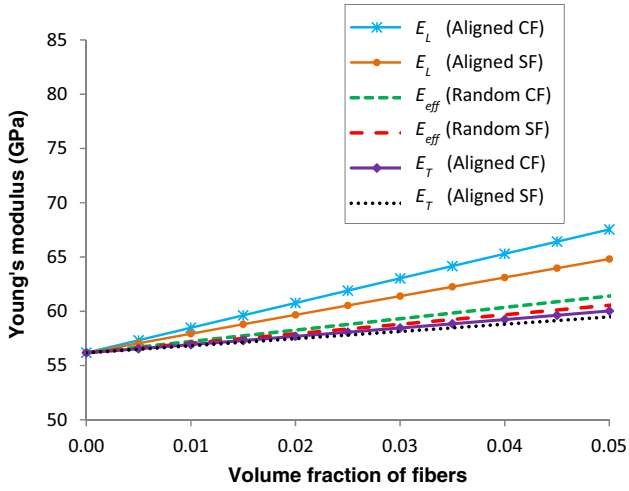

Fig. 9. Young's moduli of UHPC samples with aligned and random orientations of carbon fibers (CF) and steel fibers (SF).

Table 10
Literatures obtained input parameters for the modeling of UHPC with coarse aggregates.

Experimental data	Aggregate type	Aggregate properties			Experimental results		Model predictions
		V%	E (GPa)	υ	f_c (MPa)	E (GPa)	E (GPa)
UHPC CA-1 Esteban et al. [86]	Limestone (r_{max} = 4.7 mm)	30	65.60	0.27	141	55.75*	57.70
UHPC CA-2 Ma et al. [77]	Basalt (r_{max} = 2–5 mm)	32	54.00	0.15	150	51.00*	56.35

*indicates Ma et al.'s [60] empirical equation that accounts for the presence of coarse aggregates in UHPC is used.

formance of aligned fibers behaving as transversely isotropic material is superior to that of randomly oriented fibers. These simulation results are in agreement with the predictions from several studies [58,59], which suggest that the fiber orientation does have a significant effect on Young's modulus and the tensile and compressive properties of UHPC.

6.2. Effect of fiber geometry

The aspect ratio in this study is defined as, $\alpha = a_1/a_2$, where a_1 and a_2 are the radii of the prolate spheroid in the major and minor axis. This property was investigated by selecting three general regimes of aspect ratios, from 0.5 to 10, 10–250, and 250–2000. Then, based on these regimes, using CF with an Young's modulus of 240 GPa and Poisson's ratio of 0.2, the general trend according to which the Young's modulus and Poisson's ratio changed was computed by using the EVA method. The results are plotted in Fig. 10, which shows the change in the mechanical properties with the aspect ratio.

As Fig. 10 shows, three different trends in the change in the Young's modulus as a function of the aspect ratio become apparent. In the first range, which is for fibers with an aspect ratio ranging from 0.5 to 10, the modulus initially decreases to reach its lowest point at an aspect ratio close to 1 then increases again as the aspect ratio approaches 10. An aspect ratio of 1 generally means a spherical inclusion, which according to our analysis, is expected to provide much lower stiffness to the composite than any prolate-shaped inclusion regardless of how small the aspect ratio is.

6.3. Effect of fiber interfacial properties

It is established that slip in both the tangential and longitudinal directions becomes reduced as the surface roughness of the fibers increases. Hence, assuming perfect bonding between the hydration products and CFs can be expected to result in overestimation of the contribution of the fibers to the mechanical properties. Therefore, another homogenization is conducted for the CF reinforced UHPC by assuming a mildly weakened interface property. This homogenization uses Qu's modified Eshelby's tensor for spheroidal inclusion [59]. Then, by using the EVA method for different levels of damage in composites [55], the results presented in Fig. 9 were obtained. Computation of the modified Eshelby's tensor for the mildly weakened interface requires the compliance tensor n_{ij}, which is a function of α and β, to be sufficiently small. Therefore, for our case, we selected a range of values of α from 0 (perfect interface) to 1.00E-5 by keeping β constant at 5.00E-5 and keeping α constant at 1.00E-6 and varying B from 0 to 1. These values are selected such that they closely approximate the values proposed by Pyo and Lee [55] for their multilevel damage analysis, representing mild interface properties. Hence, the results in Fig. 11 show that application of a mild interface of compliance in the form of appropriate α and β values yields a simulation result that more closely represents the actual CF performance in the cementitious composite, and that both factors (α and β) play equally important roles to affect the performance of the material.

6.4. Effect of varying the ITZ modulus and thickness

The next parametric study we conducted was to investigate the sensitivity of the model to the effective modulus and thickness of the ITZ layer. Literature states that the Young's modulus of the ITZ should range between 40 and 60% of Young's modulus of the cement paste (E_{cement}) [64,67]. Hence, in this study the Young's modulus of the ITZ was varied from 10 to 80% of E_{cement}. The trend presented in Fig. 12 was obtained as the result. This trend shows a gradual reduction in the Young's modulus as the modulus of the ITZ was assumed much lower than the properties of the cement paste.

The thickness of the ITZ layer (t_{ITZ}) was similarly varied. Even though several researchers have suggested the ITZ thickness is not dependent on the size of the coarse aggregate, the exact thickness remains uncertain [31,67,68,72]. Therefore, the thickness of the ITZ was varied from 0.01 to 0.10 mm to investigate the general trend of its effect on the effective Young's modulus of the composite as a whole. The results, shown in Fig. 13, correspond well with the predictions made by Duplan et al. [84], who found that an increase in the thickness of the ITZ adversely affects the mechanical properties of UHPC.

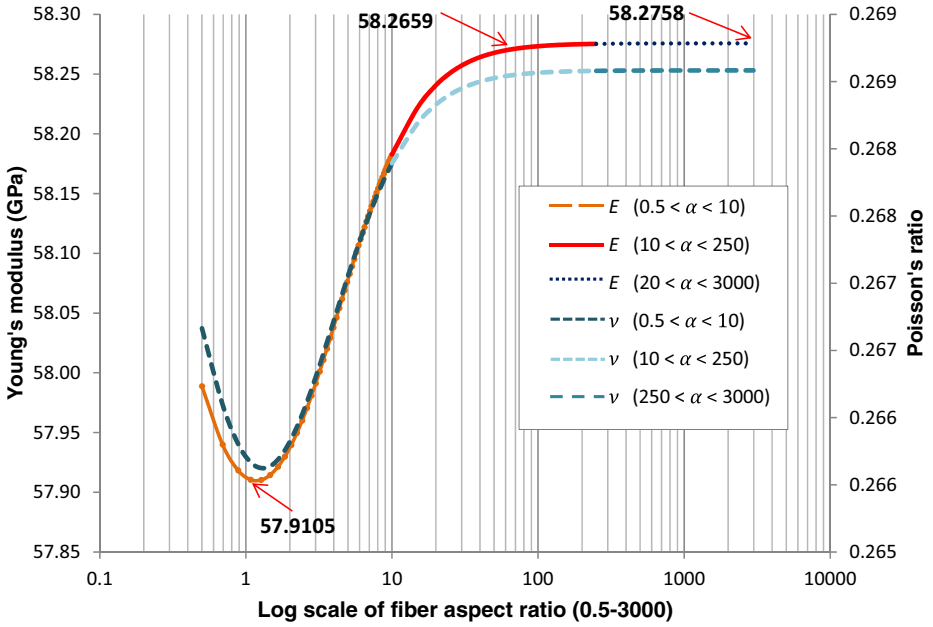

Fig. 10. General trend of the effect of the aspect ratio of fibers on UHPC's mechanical properties.

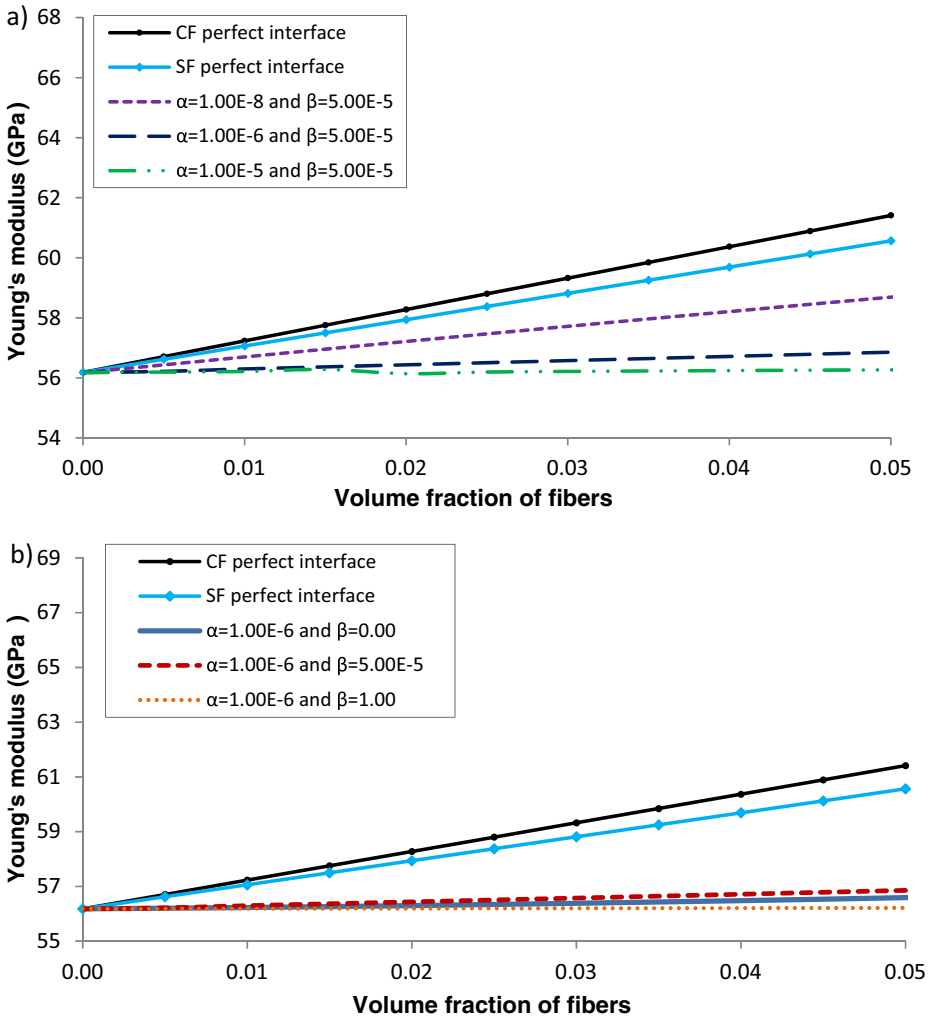

Fig. 11. Comparison of the Young's modulus (E) after applying interfacial effect on the CF by varying the compliance values α and β, (a) keeping β constant at 5.00E-5 and (b) keeping α constant at 1.00E-6.

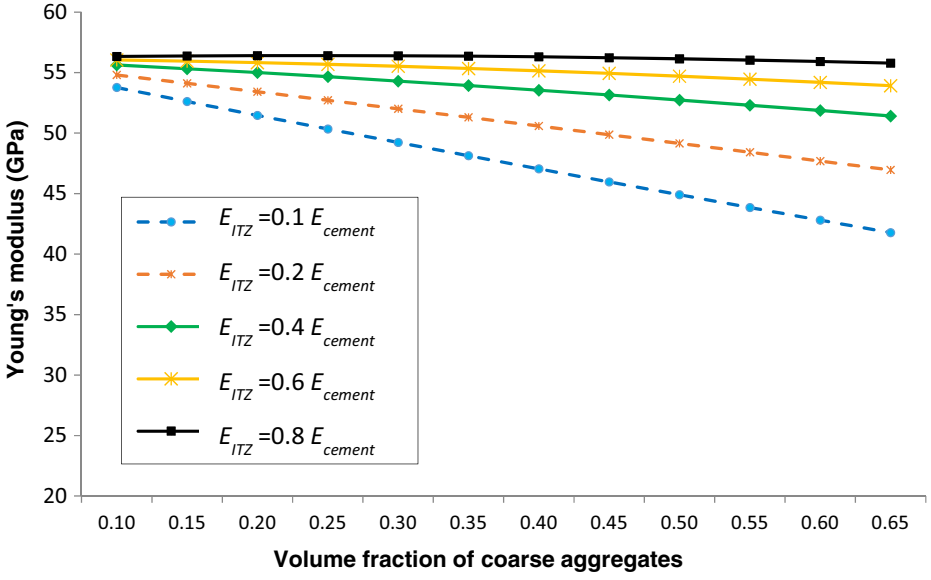

Fig. 12. Effect of the ITZ's Young's modulus on the effective modulus of UHPC as a function of the volume fraction of coarse aggregates.

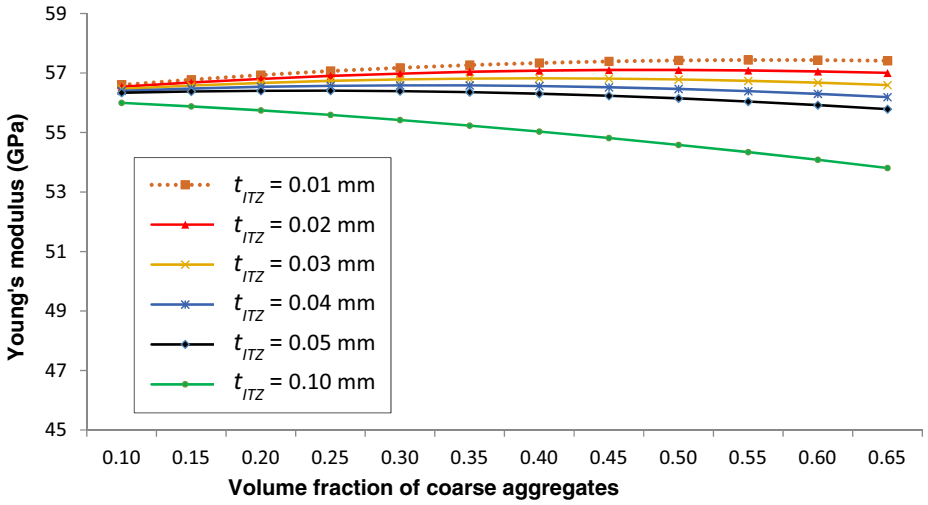

Fig. 13. Effect of the ITZ's layer thickness on the effective modulus of UHPC for varying volume fractions of the coarse aggregates.

7. Concluding remarks

This study proposed a micromechanics-based multi-level homogenization modeling scheme for the determination of the effective mechanical properties of ultra-high performance concrete (UHPC). A six-level homogenization tool was used to investigate the effects of the fiber type, geometry, orientation, aggregate sizes, aggregate volume fraction, and ITZ characteristics such as the thickness and mechanical properties. In addition, the study also examined the effect of the properties of the fiber interface on the mechanical performance of UHPC. This work also involved experimental investigations on UHPC samples to verify the assumptions made and the results. Consequently, the following conclusions can be drawn from this study.

1. For the multi-level homogenization modeling scheme, the assumption of the crystal structure of CSH as jennite crystals yields a final result of the elastic properties of UHPC that are within reasonable range of literature values.
2. The gel and capillary porosity volume fraction affect the effective mechanical properties significantly, as it was observed that they can reduce the modulus of Young's of the crystal structures of tobermorite14 Å and jennite by 50% to 35%.
3. The use of a mildly weakened interface to model the connection between CF and the UHPC matrix in the simulation yielded a more realistic value where by the SF reinforced UHPC had better mechanical properties with less porosity.
4. Investigation of the fiber type, orientation, and volume fraction showed that orientation plays an important role in the material properties. The critical aspect ratio values affecting the mechanical performance most was found to be the aspect ratio change from 1 to 50.
5. A comparison of the experimental and predicted values of UHPC with fiber showed that the values deviated by 10% to 15% whereas for coarse aggregates, the prediction showed a deviation of 7% to 15%.

This study demonstrates the applicability of the theories of micromechanics and multi-level homogenization to determine the elastic properties of cementitious composite in general and UHPC. However, as can be observed from the results and literature, UHPC is a complex material whose properties are highly influenced by the constituents. The simplifying assumptions made can have an effect on the final prediction capability of the model. Hence, in order to improve the predicting capability of the multi-level homogenization scheme, our future works will combine thermodynamic based analysis to determine the exact amount of hydration products and unreacted phases present. In addition, the model predictions showed larger deviation from the experimental results for specimens containing CF; hence, other possible causes of this deviation such as the premature rupturing of the CF during loading should be investigated. Furthermore, in this work, the elastic modulus values obtained from the simulation were compared with the elasticity values obtained from the experiments using empirical equations to determine the values. While it is true that using empirical equations is not ideal, due to the absence of experimental data for the elastic modulus values, it was decide to apply the empirically computed values. The equations have been specifically tested and developed for UHPC, with similar mix design to the one used for this study. Hence, the elastic modulus values obtained from the equations can be taken as the experimental values without creating significant error, as can be seen from the result. In addition, for future works we want to incorporate strength upscaling scheme that can determine the compressive and tensile strength properties of this material, as have been done for other cementitious composites. Moreover, micro-cracks would be modeled as either penny shaped or oblate spheroidal inclusions with interaction effects. Finally, the proposed multi-level homogenization model will be extended to incorporate the study of post peak elastoplastic damage properties of the material.

Declaration of Competing Interest

The authors declare that they have no known competing financial interests or personal relationships that could have appeared to influence the work reported in this paper.

Acknowledgement

This study was supported by a grant from the National Research Foundation of Korea (NRF) (2018R1A2A1A05076894) funded by the Korean government.

Appendix

A: MD simulation parameters

Table A1 shows the parameters of the hydration products used for the MD simulation in this study.

Table A1
MD Simulation parameters and conditions.

Simulation Parameters	Jennite	Tobermorite 14 Å	CH	Ettringite
Number of atoms	90	106	12	272
Cell size (Å) (a × b × c)	10.576 × 7.265 × 10.931	6.735 × 7.425 × 27.987	3.593 × 3.593 × 4.905	11.167 × 11.167 × 21.354
Crystal lattice type	Triclinic	Monoclinic	Trigonal	Trigonal
MD ensemble	NPT			
Forcefield	Universal(UFF)			
Temperature (K)	300			
Temperature control	Nosé-Hoover-Langevin			
Pressure (GPa)	0.001			
Pressure control	Berendsen			
Time step (fs)	1			
Total dynamic time (ns)	Until the volume of the system converges to the equilibrium quantity (1–3)			

Appendix B

EVA micromechanics

After substituting the Eshelby's tensor with an appropriate value in Eq. (1), the final effective tensor $\mathbf{C}^*$ becomes [47]

$$\mathbf{C}^* = C_{IK}^{(1)}\delta_{ij}\delta_{kl} + C_{IJ}^{(2)}\left(\delta_{ik}\delta_{jl} + \delta_{il}\delta_{jk}\right) \tag{B1}$$

in which

$$C_{IK}^{(1)} = 2\lambda_0\chi_{KK}^{(2)} + 2\mu_0\chi_{IK}^{(1)} + \sum_{n=1}^{3}\lambda_0\chi_{nK}^{(1)} \tag{B2}$$

$$C_{IJ}^{(2)} = 2\mu_0\chi_{IJ}^{(2)} \tag{B3}$$

where λ_0 is Lamme's constant for phase 0, which is the matrix phase. The components of $\chi_{IK}^{(1)}$ and $\chi_{IJ}^{(2)}$, which were derived by Pyo and Lee [85], are functions of the parameters $\Lambda_{IK}^{(2m-1)}$ and $\Lambda_{IJ}^{(2m)}$, which demonstrate progressive degradation of the interface between the inclusions and the matrix. The components of $\chi_{IK}^{(1)}$,$\chi_{IJ}^{(2)}$, $\Lambda_{IK}^{(2m-1)}$, and $\Lambda_{IJ}^{(2m)}$ are given in Pyo and Lee [55]. In this study, all the inclusions are initially modeled as though they have a perfect interface condition; hence, only the components that demonstrate perfectly bonded inclusion ($m = 1$) are considered, and the modified components for the parameters are given in Appendix C.

Appendix C

Parameters $\chi_{IK}^{(1)}$ and $\chi_{IJ}^{(2)}$ in Eqs. (B2) and (B3)

Based on the number of damage levels m (m = 1–4), $m = 1$ indicates perfectly bonded inclusion, $m = 2$ or 3 indicate a slightly and moderately debonded interface, and $m = 4$ a perfectly debonded inclusion that basically behaves as a void [55].

$$\chi_{IK}^{(1)} = \sum_{m=1}^{4}\Lambda_{IK}^{(2m-1)} = \Lambda_{IK}^{(1)} + \Lambda_{IK}^{(3)} + \Lambda_{IK}^{(5)} + \Lambda_{IK}^{(7)} \tag{C1}$$

$$\chi_{IJ}^{(2)} = \frac{1}{2} + \sum_{m=1}^{4}\Lambda_{IJ}^{(2m)} = \frac{1}{2} + \Lambda_{IJ}^{(2)} + \Lambda_{IJ}^{(4)} + \Lambda_{IJ}^{(6)} + \Lambda_{IJ}^{(8)} \tag{C2}$$

In this study, all the inclusions are initially modeled as though they have a perfect interface condition; hence, only the components that demonstrate perfectly bonded inclusion ($m = 1$) are considered and the other parts are set to zero. Hence, Eqs. (C1) and (C2) become

$$\chi_{IK}^{(1)} = \sum_{m=1}^{4}\Lambda_{IK}^{(2m-1)} = \Lambda_{IK}^{(1)} \tag{C3}$$

$$\chi_{IJ}^{(2)} = \frac{1}{2} + \sum_{m=1}^{4}\Lambda_{IJ}^{(2m)} = \frac{1}{2} + \Lambda_{IJ}^{(2)} \tag{C4}$$

For a perfectly bonded and mildly imperfect interface, $m = 1$ and 2, to become

$$\chi_{\mathrm{IK}}^{(1)} = \sum_{m=1}^{2}\Lambda_{IK}^{(2m-1)} = \Lambda_{IK}^{(1)} + \Lambda_{IK}^{(3)} \tag{C5}$$

$$\chi_{IJ}^{(2)} = \frac{1}{2} + \sum_{m=1}^{2}\Lambda_{IJ}^{(2m)} = \frac{1}{2} + \Lambda_{IJ}^{(2)} + \Lambda_{IJ}^{(4)} \tag{C6}$$

The parameters $\Lambda_{IK}^{(2m-1)}$ and $\Lambda_{IJ}^{(2m)}$, which also depend on the damage level m, are computed for $m = 1$ and $m = 2$ and given as follows,

$$\Lambda_{IK}^{(2m-1)} = \varnothing_m\left[2\eta_{IK}^{(2m-1)}\omega_{KK}^{(2m)} + 2\eta_{II}^{(2m)}\omega_{IK}^{(2m-1)} + \sum_{n=1}^{3}2\eta_{In}^{(2m-1)}\omega_{nK}^{(2m-1)}\right] \tag{C7}$$

$$\Lambda_{IK}^{(2(1)-1)} = \Lambda_{IK}^{(1)} = \varnothing_1\left[2\eta_{IK}^{(1)}\omega_{KK}^{(2)} + 2\eta_{II}^{(2)}\omega_{IK}^{(1)} + \sum_{n=1}^{3}2\eta_{In}^{(1)}\omega_{nK}^{(1)}\right] \tag{C8}$$

$$\Lambda_{IK}^{(2(2)-1)} = \Lambda_{IK}^{(3)} = \varnothing_2\left[2\eta_{IK}^{(3)}\omega_{KK}^{(4)} + 2\eta_{II}^{(4)}\omega_{IK}^{(3)} + \sum_{n=1}^{3}2\eta_{In}^{(3)}\omega_{nK}^{(3)}\right] \tag{C9}$$

$$\Lambda_{IJ}^{(2m)} = 2\varnothing_m\eta_{IJ}^{(2m)}\omega_{IJ}^{(2m)} \tag{C10}$$

$$\Lambda_{IJ}^{(2(1))} = \Lambda_{IJ}^{(2)} = 2\varnothing_1\eta_{IJ}^{(2)}\omega_{IJ}^{(2)} \tag{C11}$$

$$\Lambda_{IJ}^{(2(2))} = \Lambda_{IJ}^{(4)} = 2\varnothing_1\eta_{IJ}^{(4)}\omega_{IJ}^{(4)} \tag{C12}$$

The derivation and components of $\omega_{IK}^{(2m-1)}, \omega_{IJ}^{(2m)}, \eta_{IK}^{(2m-1)}$, and $\eta_{IJ}^{(2m)}$ are given in [55] and their modifications for $m = 1$ are given as follows,

$$\omega_{IK}^{(2m-1)} = \frac{\Gamma_{\mathrm{IK}}^{(\mathrm{m})}}{1 - 2\xi_{II}^{(2m)}} \text{ and } \omega_{IJ}^{(2m)} = \frac{1}{2 - 4\xi_{IJ}^{(2m)}} \tag{C13}$$

$$\omega_{IK}^{(1)} = \frac{\Gamma_{\mathrm{IK}}^{(1)}}{1 - 2\xi_{II}^{(2)}} \text{ and } \omega_{IJ}^{(2)} = \frac{1}{2 - 4\xi_{IJ}^{(2)}} \tag{C14}$$

Then $\Gamma_{IK}^{(m)}$ defined in [55] can be modified for $m = 1$ to give,

$$\Gamma_{\mathrm{I1}}^{(1)} = \frac{\left[\frac{1}{2} - \xi_{22}^{(1)} - \xi_{22}^{(2)}\right]\xi_{\mathrm{I1}}^{(1)} + \xi_{21}^{(1)}\xi_{\mathrm{I2}}^{(1)}}{\left[\frac{1}{2} - \xi_{22}^{(1)} - \xi_{22}^{(2)}\right]\left[1 - \xi_{11}^{(1)} - 2\xi_{11}^{(2)}\right] - \xi_{12}^{(1)}\xi_{21}^{(1)}} \tag{C15}$$

$$\Gamma_{12}^{(1)} = \Gamma_{13}^{(1)} = \frac{\left[1 - \xi_{11}^{(1)} - 2\xi_{11}^{(2)}\right]\xi_{12}^{(1)} + \xi_{12}^{(1)}\xi_{11}^{(1)}}{2\left[\frac{1}{2} - \xi_{22}^{(1)} - \xi_{22}^{(2)}\right]\left[1 - \xi_{11}^{(1)} - 2\xi_{11}^{(2)}\right] - 2\xi_{12}^{(1)}\xi_{21}^{(1)}} \tag{C16}$$

where $\xi_{IK}^{(2m-1)}$ and $\xi_{IJ}^{(2m)}$ defined in [55] can be modified for $m = 1$ to give,

$$\xi_{IK}^{(1)} = \frac{\varnothing_1}{4(1-\nu_0)}\left[2S_{IK}^{(1)}\eta_{KK}^{(2)} + 2S_{II}^{(2)}\eta_{IK}^{(1)} + \sum_{n=1}^{3} S_{In}^{(1)}\eta_{nK}^{(1)}\right] \tag{C17}$$

$$\xi_{IJ}^{(2)} = \frac{\varnothing_1 S_{IJ}^{(2)}\eta_{IJ}^{(2)}}{2(1-\nu_0)} \tag{C18}$$

with $\eta_{IK}^{(2m-1)}$ and $\eta_{IJ}^{(2m)}$ as given in [55] are also computed for $m = 1$ and are as follows

$$\eta_{IK}^{(1)} = \frac{2(1-\nu_0)\psi_{IK}^{(1)}}{\mu'_1 + S_{II}^{(2)}} \tag{C19}$$

$$\eta_{IJ}^{(2)} = \frac{(1-\nu_0)}{\mu'_1 + S_{IJ}^{(2)}} \tag{C20}$$

where the fourth-order tensor $(\psi_{IK}^{(1)})$ is given by:

$$\psi_{11}^{(1)} = \frac{\left[\lambda'_1 + \mu'_1 + S_{22}^{(1)} + S_{22}^{(2)}\right]\left[\lambda'_1 + S_{11}^{(1)}\right] - \left[\lambda'_1 + S_{21}^{(1)}\right]\left[\lambda'_1 + S_{12}^{(1)}\right]}{\left[\lambda'_1 + \mu'_1 + S_{22}^{(1)} + S_{22}^{(2)}\right]\left[\lambda'_1 + 2\mu'_1 + S_{11}^{(1)} + 2S_{11}^{(2)}\right] - \left[\lambda'_1 + S_{12}^{(1)}\right]\left[\lambda'_1 + S_{21}^{(1)}\right]} \tag{C21}$$

$$\psi_{12}^{(1)} = \psi_{13}^{(1)} = \frac{\left[\lambda'_1 + 2\mu'_1 + S_{11}^{(1)} + 2S_{11}^{(2)}\right]\left[\lambda'_1 + S_{12}^{(1)}\right] - \left[\lambda'_1 + S_{12}^{(1)}\right]\left[\lambda'_1 + S_{11}^{(1)}\right]}{2\left[\lambda'_1 + \mu'_1 + S_{22}^{(1)} + S_{22}^{(2)}\right]\left[\lambda'_1 + 2\mu'_1 + S_{11}^{(1)} + 2S_{11}^{(2)}\right] - 2\left[\lambda'_1 + S_{12}^{(1)}\right]\left[\lambda'_1 + S_{21}^{(1)}\right]} \tag{C22}$$

Finally, λ'_m and μ'_m can be computed from:

$$\lambda'_m = \frac{4(1-\nu_0)(\mu_m\lambda_0 - \mu_0\lambda_m)}{(\mu_m - \mu_0)\left[3(\lambda_m - \lambda_0) + 2(\mu_m - \mu_0)\right]} \tag{C23}$$

$$\mu'_m = \frac{2\mu_0(1-\nu_0)}{(\mu_m - \mu_0)} \tag{C24}$$

References

[1] C. Shi, Z. Wu, J. Xiao, D. Wang, Z. Huang, Z. Fang, A review on ultra high performance concrete : part I. Raw materials and mixture design, Constr. Build. Mater. 101 (2015) 741–751, https://doi.org/10.1016/j.conbuildmat.2015.10.088.

[2] P. Richard, M. Cheyrezy, Composition of reactive powder concretes, Cem. Concr. Res. 25 (1995) 1501–1511, https://doi.org/10.1016/0008-8846(95)00144-2.

[3] B.A. Graybeal, Characterization of the behavior of UHPC, University of Maryland, 2005.

[4] S. Rahman, T. Molyneaux, I. Patnaikuni, Ultra High Performance Concrete (UHPC), Aust. J. Civ. Eng. 2 (2005), https://doi.org/10.1080/14488353.2005.11463913.

[5] H.G. Russel, B.A. Graybeal, Ultra-High Performance Concrete : A State-of-the-Art Report for the Bridge Community, 2013. doi:FHWA-HRT-13-060.

[6] Y.J. Kim, Recent Advances in Ultra-high Performance Concrete, J. Korean Recycl. Constr. Resour. Inst. 1 (2013) 163–172, https://doi.org/10.14190/JRCR.2013.1.3.163.

[7] N.J. Mattei, M.M. Mehrabadi, H. Zhu, A micromechanical constitutive model for the behavior of concrete, Mech. Mater. 39 (2007) 357–379, https://doi.org/10.1016/j.mechmat.2006.05.007.

[8] M.M. Reda, N.G. Shrive, J.E. Gillott, Microstructural investigation of innovative UHPC, Cem. Concr. Res. 29 (1999) 323–329, https://doi.org/10.1016/S0008-8846(98)00225-7.

[9] M.I. Okereke, A.I. Akpoyomare, M.S. Bingley, Virtual testing of advanced composites, cellular materials and biomaterials: a review, Compos. Part B Eng. 60 (2014) 637–662, https://doi.org/10.1016/j.compositesb.2014.01.007.

[10] A. Le Hoang, E. Fehling, Influence of steel fiber content and aspect ratio on the uniaxial tensile and compressive behavior of ultra high performance concrete, Constr. Build. Mater. 153 (2017) 790–806, https://doi.org/10.1016/j.conbuildmat.2017.07.130.

[11] K.S.E.-D. Hamdy, H.A. Mohamed, M.A. El-Hak Khater, S. Ahmed, Effect of Steel Fibers on Behavior of Ultra High Performance Concrete, in: First Int. Interact. Symp. UHPC, 2016: pp. 1–10.

[12] N. Hicks, Fiber Orientation in Ultra-High-Performance Concrete (UHPC) Shear Connections in Adjacent Box Beam Bridges, Ohio University, 2015.

[13] B. Zhou, Y. Uchida, Fiber Orientation in Ultra High Performance Fiber Reinforced Concrete and Its Visualization, VIII Int. Conf. Fract. Mech. Concr. Concr. Struct. Fram. (2013) 1–8.

[14] S.J. Barnett, J.-F. Lataste, T. Parry, S.G. Millard, M.N. Soutsos, Assessment of fibre orientation in ultra high performance fibre reinforced concrete and its effect on flexural strength, Mater. Struct. 43 (2010) 1009–1023, https://doi.org/10.1617/s11527-009-9562-3.

[15] D.Y. Yoo, Y.S. Yoon, Structural performance of ultra-high-performance concrete beams with different steel fibers, Eng. Struct. 102 (2015) 409–423, https://doi.org/10.1016/j.engstruct.2015.08.029.

[16] S. He, J. Qiu, J. Li, E.H. Yang, Strain hardening ultra-high performance concrete (SHUHPC) incorporating CNF-coated polyethylene fibers, Cem. Concr. Res. 98 (2017) 50–60, https://doi.org/10.1016/j.cemconres.2017.04.003.

[17] D.J. Kim, S.H. Park, G.S. Ryu, K.T. Koh, Comparative flexural behavior of Hybrid Ultra High Performance Fiber Reinforced Concrete with different macro fibers, Constr. Build. Mater. 25 (2011) 4144–4155, https://doi.org/10.1016/j.conbuildmat.2011.04.051.

[18] Y.S. Tai, S. El-Tawil, T.H. Chung, Performance of deformed steel fibers embedded in ultra-high performance concrete subjected to various pullout rates, Cem. Concr. Res. 89 (2016) 1–13, https://doi.org/10.1016/j.cemconres.2016.07.013.

[19] L. Sorelli, G. Constantinides, F.J. Ulm, F. Toutlemonde, The nano-mechanical signature of Ultra High Performance Concrete by statistical nanoindentation techniques, Cem. Concr. Res. 38 (2008) 1447–1456, https://doi.org/10.1016/j.cemconres.2008.09.002.

[20] S. Zhao, W. Sun, Nano-mechanical behavior of a green ultra-high performance concrete, Constr. Build. Mater. 63 (2014) 150–160, https://doi.org/10.1016/j.conbuildmat.2014.04.029.

[21] N. Van Tuan, G. Ye, K. Van Breugel, O. Copuroglu, Hydration and microstructure of ultra high performance concrete incorporating rice husk ash, Cem. Concr. Res. 41 (2011) 1104–1111, https://doi.org/10.1016/j.cemconres.2011.06.009.

[22] O. Bernard, F.J. Ulm, E. Lemarchand, A multiscale micromechanics-hydration model for the early-age elastic properties of cement-based materials, Cem. Concr. Res. 33 (2003) 1293–1309, https://doi.org/10.1016/S0008-8846(03)00039-5.

[23] W.R.L. Da Silva, J. Němeček, P. Štemberk, Application of multiscale elastic homogenization based on nanoindentation for high performance concrete, Adv. Eng. Softw. 62–63 (2013) 109–118, https://doi.org/10.1016/j.advengsoft.2013.04.007.

[24] M. Schmidt, E. Fehling, Ultra-high-performance concrete: Research, development and application in Europe, in: Seventh Int. Symp. Util. High Strength/High-Performance Concr. (2005) 51–78. http://download.contec-aps.com/uploads/tx_mpdownloadcenter/pp_fp_2005_003_eng_01.pdf.

[25] J.T. Oden, T. Belytschko, I. Babuska, T.J.R. Hughes, Research directions in computational mechanics, Comput. Methods Appl. Mech. Eng. 192 (2003) 913–922, https://doi.org/10.1016/S0045-7825(02)00616-3.

[26] P. Kabele, Multiscale framework for modeling of fracture in high performance fiber reinforced cementitious composites, Eng. Fract. Mech. 74 (2007) 194–209, https://doi.org/10.1016/j.engfracmech.2006.01.020.

[27] L. Contrafatto, M. Cuomo, L. Greco, Meso-scale simulation of concrete multiaxial behaviour, Eur. J. Environ. Civ. Eng. 21 (2017) 896–911, https://doi.org/10.1080/19648189.2016.1182085.

[28] S.Y. Kim, H.G. Jang, C.M. Yang, B. Yang, Multiscale prediction of thermal conductivity for nanocomposites containing crumpled carbon nanofillers with interfacial characteristics, Compos. Sci. Tech. 155 (2018) 169–176.

[29] B.J. Yang, H. Souri, S. Kim, S. Ryu, H.K. Lee, An analytical model to predict curvature effects of the carbon nanotube on the overall behavior of nanocomposites, J. Appl. Phys. 117 (2015) 119901.

[30] H. Jeon, J. Yu, H. Lee, G.M. Kim, J.W. Kim, Y.C. Jung, C.-M. Yang, B.J. Yang, A combined analytical formulation and genetic algorithm to analyze the nonlinear damage responses of continuous fiber toughened composites, Comput. Mech. 60 (2017) 393–408.

[31] H.M. Park, S.M. Park, S. Lee, I. Shon, H. Jeon, B.J. Yang, Automated generation of carbon nanotube morphology in cement composite via data-driven approaches, Compos. Part B Eng. 167 (2019) 51–62. doi:S1359836818322637.

[32] G. Li, Y. Zhao, S.S. Pang, Four-phase sphere modeling of effective bulk modulus of concrete, Cem. Concr. Res. 29 (1999) 839–845, https://doi.org/10.1016/S0008-8846(99)00040-X.

[33] G. Li, Y. Zhao, S.S. Pang, Y. Li, Effective Young's modulus estimation of concrete, Cem. Concr. Res. 29 (1999) 1455–1462, https://doi.org/10.1016/S0008-8846(99)00119-2.

[34] P. Simeonov, S. Ahmad, Effect of transition zone on the elastic behavior of cement-based composites, Cem. Concr. Res. 25 (1995) 165–176, https://doi.org/10.1016/0008-8846(94)00124-H.

[35] A. Al-Ostaz, W. Wu, A.H.D. Cheng, C.R. Song, A molecular dynamics and microporomechanics study on the mechanical properties of major constituents of hydrated cement, Compos. Part B Eng. 41 (2010) 543–549, https://doi.org/10.1016/j.compositesb.2010.06.005.
[36] G. Constantinides, F.J. Ulm, The effect of two types of C-S-H on the elasticity of cement-based materials: results from nanoindentation and micromechanical modeling, Cem. Concr. Res. 34 (2004) 67–80, https://doi.org/10.1016/S0008-8846(03)00230-8.
[37] P.D. Tennis, H.M. Jennings, Model for two types of calcium silicate hydrate in the microstructure of Portland cement pastes, Cem. Concr. Res. 30 (2000) 855–863, https://doi.org/10.1016/S0008-8846(00)00257-X.
[38] A.C.A. Muller, K.L. Scrivener, A.M. Gajewicz, P.J. McDonald, Densification of C-S-H measured by 1H NMR relaxometry, J. Phys. Chem. C. 117 (2013) 403–412, https://doi.org/10.1021/jp3102964.
[39] M. Königsberger, C. Hellmich, B. Pichler, Densification of C-S-H is mainly driven by available precipitation space, as quantified through an analytical cement hydration model based on NMR data, Cem. Concr. Res. 88 (2016) 170–183, https://doi.org/10.1016/j.cemconres.2016.04.006.
[40] M. Königsberger, M. Hlobil, B. Delsaute, S. Staquet, C. Hellmich, B. Pichler, Hydrate failure in ITZ governs concrete strength: a micro-to-macro validated engineering mechanics model, Cem. Concr. Res. 103 (2018) 77–94, https://doi.org/10.1016/j.cemconres.2017.10.002.
[41] B. Pichler, C. Hellmich, J. Eberhardsteiner, J. Wasserbauer, P. Termkhajornkit, R. Barbarulo, G. Chanvillard, Effect of gel-space ratio and microstructure on strength of hydrating cementitious materials: an engineering micromechanics approach, Cem. Concr. Res. 45 (2013) 55–68, https://doi.org/10.1016/j.cemconres.2012.10.019.
[42] B. Pichler, C. Hellmich, Upscaling quasi-brittle strength of cement paste and mortar: a multi-scale engineering mechanics model, Cem. Concr. Res. 41 (2011) 467–476, https://doi.org/10.1016/j.cemconres.2011.01.010.
[43] W.R.L. Silva, J. Nemecek, S. P.,, Methodology for nanoindentation-assisted prediction of macroscale elastic properties of high performance cementitious composites, Cem. Concr. Compos. 45 (2014) 57–68, https://doi.org/10.1016/j.cemconcomp.2013.09.013.
[44] J. Zhang, Y. Zhao, The mechanical properties and microstructure of ultra-high-performance concrete containing various supplementary cementitious materials, J. Sustain. Cem. Mater. 6 (2017) 254–266, https://doi.org/10.1080/21650373.2016.1262798.
[45] Y. Zhang, Z. Yan, J.W. Ju, H. Zhu, Q. Chen, A multi-level micromechanical model for elastic properties of hybrid fiber reinforced concrete, Constr. Build. Mater. 152 (2017) 804–817, https://doi.org/10.1016/j.conbuildmat.2017.07.024.
[46] T. Mori, K. Tanaka, Average stress in matrix and average elastic energy of materials with misfitting inclusions, Acta Metall. 21 (1973) 571–574, https://doi.org/10.1016/0001-6160(73)90064-3.
[47] J.W. Ju, T.M. Chen, Micromechanics and effective moduli of elastic composites containing randomly dispersed ellipsoidal inhomogeneities, Acta Mech. 103 (1994) 103–121, https://doi.org/10.1007/BF01180221.
[48] R.M. Christensen, K.H. Lo, Solutions for effective shear properties in three phase sphere and cylinder models, J. Mech. Phys. Solids. 27 (1979) 315–330, https://doi.org/10.1016/0022-5096(79)90032-2.
[49] S. Hajilar, Nano-Scale Investigation of Mechanical Characteristics of Main Phases of Hydrated Cement Paste, University of Massachusetts Amherst, 2015.
[50] G. Constantinides, F.J. Ulm, The nanogranular nature of C-S-H, J. Mech. Phys. Solids. 55 (2007) 64–90, https://doi.org/10.1016/j.jmps.2006.06.003.
[51] E. Abdolhosseini Qomi, M. J. Masoero, M. Bauchy, F.-J. Ulm, C-S-H across Length Scales: From Nano to Micron, in: 10th Int. Conf. Mech. Phys. Creep, Shrinkage, Durab. Concr. Concr. Struct., Vienna, Austria, September 21-23, 2015, n.d.: pp. 39–48.
[52] R.J.-M. Pellenq, A. Kushima, R. Shahsavari, K.J. Van Vliet, M.J. Buehler, S. Yip, F.-J. Ulm, A realistic molecular model of cement hydrates, Proc. Natl. Acad. Sci. 106 (2009) 16102–16107, https://doi.org/10.1073/pnas.0902180106.
[53] M. Vandamme, F.J. Ulm, P. Fonollosa, Nanogranular packing of C-S-H at substochiometric conditions, Cem. Concr. Res. 40 (2010) 14–26, https://doi.org/10.1016/j.cemconres.2009.09.017.
[54] J. Qu, M. Cherkaoui, Fundamentals of micromechanics of solids (2015), https://doi.org/10.1007/978-1-84996-335-0_4.
[55] S.H. Pyo, H.K. Lee, Micromechanical analysis of aligned and randomly oriented whisker-/ short fiber-reinforced composites, Cmes. 40 (2009) 271–305.
[56] G.M. Odegard, T.S. Gates, K.E. Wise, C. Park, E.J. Siochi, Constitutive modeling of nanotube-reinforced polymer composites, Compos. Sci. Technol. 63 (2003) 1671–1687, https://doi.org/10.1016/S0266-3538(03)00063-0.
[57] N. Marzari, M. Ferrari, Textural and Micromorphological Effects on the Overall Elastic Response of Macroscopically Anisotropic Composites, ASME. J. Appl. Mech. 59 (1992) 269–275.
[58] H.K. Lee, S. Simunovic, Modeling of progressive damage in aligned and randomly oriented discontinuous fiber polymer matrix composites, Compos. Part B Eng. 31 (2000) 77–86, https://doi.org/10.1016/S1359-8368(99)00070-0.
[59] J. Qu, Eshelby Tensor for an Elastic Inclusion With Slightly Weakened Interface, J. Appl. Mech. 60 (1993) 1048–1050, https://doi.org/10.1115/1.2900974.
[60] H. Ma, Multi-scale Modeling of the Microstructure and Transport Properties of Contemporary Concrete, The Hong Kong University of Science and Technology, 2013.
[61] A.M. Brandt, Cement-Based Composites Second Edition, 2nd, 1995.
[62] R. Yu, P. Spiesz, H.J.H. Brouwers, Mix design and properties assessment of Ultra-High Performance Fibre Reinforced Concrete (UHPFRC), Cem. Concr. Res. 56 (2014) 29–39, https://doi.org/10.1016/j.cemconres.2013.11.002.
[63] G. Geng, R.J. Myers, M.J.A. Qomi, P.J.M. Monteiro, Densification of the interlayer spacing governs the nanomechanical properties of calcium-silicate-hydrate, Sci. Rep. 7 (2017), https://doi.org/10.1038/s41598-017-11146-8.
[64] H.M. Jennings, Colloid model of C–S–H and implications to the problem of creep and shrinkage, Mater. Struct. 37 (2004) 59–70, https://doi.org/10.1007/BF02481627.
[65] D. Jagannathan, Calcium-Silicate-Hydrate in cementitious systems: chemomechanical correlations, extreme temperature behavior, and kinetics and morphology of in-situ formation, Massachusetts Institute of Technology (2013).
[66] S. Speziale, F. Jiang, Z. Mao, P.J.M. Monteiro, H.R. Wenk, T.S. Duffy, F.R. Schilling, Single-crystal elastic constants of natural ettringite, Cem. Concr. Res. 38 (2008) 885–889, https://doi.org/10.1016/j.cemconres.2008.02.004.
[67] G. Bumanis, N. Toropovs, L. Dembovska, D. Bajare, A. Korjakins, The Effect of Heat Treatment on the Properties of Ultra High Strength Concrete, in: 10th Int. Sci. Pract. Conf., 2015: pp. 22–27.
[68] S.H. Kang, J.H. Lee, S.G. Hong, J. Moon, Microstructural investigation of heat-treated ultra-high performance concrete for optimum production, Materials (Basel). 10 (2017), https://doi.org/10.3390/ma10091106.
[69] B.J. Yang, S.K. Ha, S.H. Pyo, H.K. Lee, Mechanical characteristics and strengthening effectiveness of random-chopped FRP composites containing air voids, Compos. Part B Eng. 62 (2014) 159–166, https://doi.org/10.1016/j.compositesb.2014.02.015.
[70] K. van Breugel, Y. Guang, Analyses of hydration processes and microstructural development of UHPC through numerical simulation, in: Int. Symp. Ultra High Perform. Concr., n.d.: pp. 253–264.
[71] O. Bonneau, C. Poulin, J. Dugat, P. Richard, P. Aitcin, Reactive powder concretes: from theory to practice, Concr. Int. 18 (1996) 47–49.
[72] S.M. Park, B. Yang, H. Jeon, A computational framework for quantifying reactivity of fly ash in cement pastes from backscattered electron images, Constr. Build. Mater. 200 (2019) 630–636.
[73] W. Pansuk, H. Sato, Y. Sato, R. Shionaga, Tensile Behaviors and Fiber Orientation of UHPC, in: Second Int. Symp. Ultra-High Perform. Concr., 2008: pp. 161–168.
[74] H.W. Wang, H. Zhou, L. Gui, H. Ji, X. Zhang, Analysis of Fiber Orientation on Young's Modulus for Unidirectional Fiber Reinforced Composites, Compos. Part B, Eng. 56 (2014) 733–739.
[75] S. Mindess, Interface in Concrete, J.P, Skaln. (Ed.), Mater. Sci. Concr. Am. Ceram. Soc. (1989) 163–180.
[76] M.P. Lutz, P.J. Monteiro, R.W. Zimmerman, Inhomogeneous interfacial transition zone model for the bulk modulus of mortar, Cem. Concr. 27 (1997) 1113–1122.
[77] J. Ma, M. Orgass, F. Dehn, D. Schmidt, N.V. Tue, Comparative Investigations on Ultra-High Performance Concrete with or without Coarse Aggregates, Proc. Int. Symp. Ultra High Perform. Concr. Kassel. (2004) 205–212.
[78] W.A. Tasong, C.J. Lynsdale, C. Cripps, Aggregate-cement paste interface. II: Influence of aggregate physical properties, Cem. Concr. Res. 28 (1998) 1453–1465.
[79] Comité Euro-International du Béton, High-Performance Concrete, Recommended Extensions to the Model Code 90–Research Needs, 1995.
[80] E. 1992-1-1, Eurocode 2. Design of Concrete Structures—Part 1: General Rules and Rules for Buildings, 2004.
[81] A.C. 363, State-of-the-Art Report on High-Strength Concrete, in: ACI JOURNAL, Proc., 1984: pp. 364–411.
[82] T. Noguchi, F. Tomosawa, K.M. Nemati, B.M. Chiaia, A.P. Fantilli, A Practical Equation for Elastic Modulus of Concrete, ACI Struct. J. 106 (2009) 690.
[83] G.M. Kim, B.J. Yang, H.N. Yoon, H.K. Lee, Synergistic effects of carbon nanotube and carbon fiber on heat generation and electrical characteristics of cementitious composites, Carbon N. Y. 134 (2018) 283–292, https://doi.org/10.1016/j.carbon.2018.03.070.
[84] F. Duplan, A. Abou-Chakra, A. Turatsinze, G. Escadeillas, S. Brule, F. Masse, Prediction of modulus of elasticity based on micromechanics theory and application to low-strength mortars, Constr. Build. Mater. 50 (2014) 437–447, https://doi.org/10.1016/j.conbuildmat.2013.09.051.
[85] H. Lee, S. Pyo, 3D-damage model for fiber-reinforced brittle composites with microcracks and imperfect interfaces, J. Eng. Mech. 135 (2009) 1108–1118, https://doi.org/10.1061/(ASCE)EM.1943-7889.0000039.
[86] C. Esteban, J.A. Lopes, P.S. Ros, Definitions of three levels of performance for UHPCFRC-VHPFRC with available materials, in: Proc. Hipermat 2012 3rd Int. Symp. UHPC Nanotechnol. High Perform. Constr. Mater., n.d.: pp. 249–256.